Vibration Attenuation for Satellite Reaction Wheels through the use of Field-Oriented Control

Linnéa Rosenbecker

LUND UNIVERSITY

Department of Automatic Control

MSc Thesis
TFRT-6119
ISSN 0280-5316

Department of Automatic Control
Lund University
Box 118
SE-221 00 LUND
Sweden

Printed in Sweden by Tryckeriet i E-huset
Lund 2020

Abstract

Complex space components are getting more important as the request for high precision space missions is increasing. The main contribution to vibrations on a satellite is the reaction wheels, the primary actuator in the attitude control of the satellite. One of the main sources of vibrations is torque ripple which is caused by various reasons, one being the control algorithm. This thesis focuses on reducing the vibrations in the reaction wheels at Hyperion Technologies by using a more complex motor control algorithm known as field-oriented control (FOC) instead of six-step commutation that is currently used. The reaction wheel driven with FOC was simulated in Python before testing the concept on the real reaction wheel. The open-source electronic speed controller VESC was used to evaluate the performance of the reaction wheel driven with FOC. The results from the simulations showed that it would be a significant improvement to use FOC, both when it comes to torque ripple and control performance. Due to some difficulties with the vibration measurement setup, the torque ripple aspect of the controller could not be confirmed in real life. It has, however, been shown that the reaction wheel would greatly advantage from using FOC instead of six-step commutation when it comes to the control performance.

Acknowledgements

I could not have finished this thesis without the support from a few people. I am very grateful to everyone at Hyperion Technologies. They have taught me a lot, always helped me when I have needed it and made me feel welcome. I have had a great time at the company. A special thanks to Bert Monna, my supervisor at the company, for giving me the opportunity to do this Master's thesis and for all the support. He has spent hours explaining things to me, even topics not related to this project just to satisfy my curiosity. Further, I would like to thank my supervisor Anders Robertsson at the Department of Automatic Control for his support and guidance during this thesis and for not giving up on finding a way to get the vibration measurements. I would also like to thank my examiner Kristian Soltez, for his ideas and advice, and everyone else who have been involved in this project in some way. Lastly, I would like to express my gratitude towards my friends and family who have made sure to keep me motivated through this thesis.

Contents

1. Introduction **9**

1.1 Background 9

1.2 Aim of the Thesis 10

1.3 Strategy 11

2. Reaction Wheels and Electric Motors **12**

2.1 Introduction to Reaction Wheels 12

2.2 Brushless DC Motor 14

2.3 Reference Frames 16

2.4 Mathematical Model 18

2.5 Mathematical Model in the dq-Frame 24

2.6 State Estimation 24

2.7 Three-Phase Inverter 25

2.8 Commutation 27

2.9 Torque Ripple 30

3. Field-Oriented Control **32**

3.1 Fundamentals of FOC 32

3.2 PI Controller 34

3.3 Current Controllers 35

3.4 Speed Controller 37

3.5 Space Vector Pulse Width Modulation 37

4. Implementation **42**

4.1 Introduction to VESC 42

4.2 Running the Reaction Wheel with VESC 44

4.3 Hall Sensor Table 45
4.4 Current Controller Tuning 45
4.5 Alterations in the Firmware 46
4.6 Speed Controller Tuning 46
5. Experiments and Results **49**
5.1 Results from the Python Simulation 49
5.2 Results from the Hardware Implementation 54
5.3 Vibration Testing 59
6. Discussion **63**
6.1 Controller Performance 63
6.2 Vibrations 65
6.3 Future Work 66
7. Conclusions **68**
Bibliography **69**

1

Introduction

1.1 Background

Reaction wheels are common actuators in the attitude control system of satellites, providing the necessary torque to reach a desired orientation and stability. They are based on the conservation of angular momentum. Applying torque to the wheel in one direction will result in the satellite moving in the opposite direction, in accordance with the principle of angular momentum conservation. Reaction wheels are, however, the main disturbance source onboard the satellite as they induce micro-vibrations. High control accuracy of the reaction wheels is therefore important to meet the required pointing accuracy of the satellite.

Hyperion Technologies is a company in Delft, the Netherlands, focusing on the design of products for small spacecraft, where they among other things provide reaction wheels. The reaction wheel used in this thesis will be the RW400 reaction wheel, shown in Figure 1.1.

Reaction wheels are critical due to bearings and vibrations. One of the main contributions of the vibrations of the reaction wheels is torque ripple. This effect can be reduced with a suitable choice of control method. Currently, the reaction wheels at Hyperion Technologies make use of six-step commutation in their control algorithm, which is known to result in more torque ripple than other common methods for motor drive. This method is simple to understand and to implement on hardware. The drawback,

however, is that the current space vector can only have six directions, making it sometimes misaligned from the optimal direction. This causes torque ripple but also loss in efficiency. Field-oriented control (FOC) is a motor drive method that is known to result in far less torque ripple compared to six-step commutation since it always aims at using the optimal direction of the current vector. As a consequence, however, it consists of more complex calculations. It is desired to investigate whether field-oriented control will improve the performance of the reaction wheel or not.

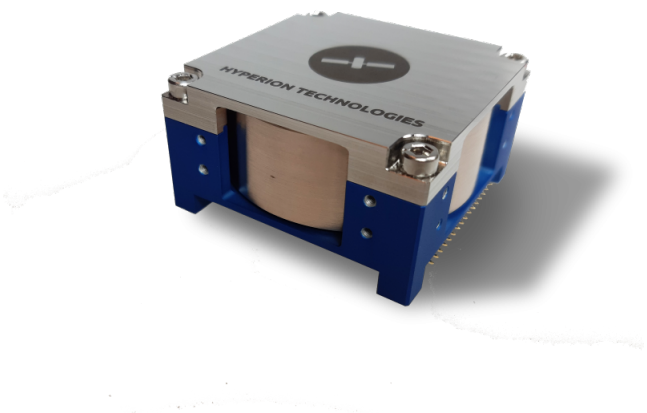

Figure 1.1: *The Hyperion Technologies RW400 reaction wheel. (Image courtesy of Hyperion Technologies.)*

1.2 Aim of the Thesis

This thesis aims at designing a field-oriented control scheme for the control of the RW400 reaction wheel, to analyse the performance, and to compare the control method with the current method in terms of performance and the amount of micro-vibrations they result in. The developed control algorithm should be able to operate in the full speed range, including zero-crossings. The aim is to have a controller that results in less micro-vibrations due to torque ripple and that have a more efficient performance.

1.3 Strategy

To improve the performance and micro-vibrations of the reaction wheel, the first step will be to simulate the reaction wheel driven with six-step commutation and field-oriented control using Python. After obtaining an understanding of the system and after developing the controller in Python, the FOC scheme will be tested on real hardware. For this, the open-source electronic speed controller VESC will be used. This hardware comes with open-source firmware with FOC. Since it is open-source, it can easily be modified if necessary. When the implementation on the real reaction wheel is finalised, the performance will be analysed in terms of step responses and current consumption. Finally, the micro-vibrations will be measured using a Kistler table. The measurements will be done using both the current Hyperion Technologies reaction wheel controller and the VESC controller with FOC to compare the performance of the two.

2

Reaction Wheels and Electric Motors

Electric motors are being used in a wide range of applications, from hard disk drives to vacuum cleaners and all the way to outer space for driving reaction wheels. They are based on the conversion of electrical energy to magnetic energy, and lastly to mechanical energy. In this chapter, the theory behind reaction wheels driven by electric motors, and in particular brushless motors, will be explained.

2.1 Introduction to Reaction Wheels

Reaction wheels are an important component in satellites as the primary actuator in the attitude control system, especially where high pointing accuracy is needed. They are typically composed of a brushless direct current (BLDC) motor attached to a high inertia flywheel. The reaction wheel is in turn attached to the spacecraft and provide attitude control through angular momentum exchange with the spacecraft [Lopes et al., 2019]. Since the torques and forces used to spin up the wheel are internal to the system, the angular momentum is conserved. Therefore, the angular momentum of the satellite is equal in magnitude in the opposite direction of the accumulated angular momentum in the wheel. Torque is proportional to the electric current so by adjusting the current to the electric motor the reaction wheel will speed up or slow down and produce torque. An opposite torque will be

applied to the satellite, consequently rotating it and adjusting its attitude in one axis [Mohamad et al., 2015]. For three-axis control, at least three reaction wheels mounted perpendicular to each other are required. It is also common to use four reaction wheels along tetrahedral axes for redundancy, in case one of the reaction wheels would stop functioning.

Satellites in space are subject to perturbing forces. These could come from solar pressure, atmospheric drag or celestial bodies. The attitude control system on the satellite receives information about the attitude from inertial sensors like star trackers, magnetometers, gyroscopes and sun sensors. Based on this information the attitude control actuators can move the satellite towards the desired attitude as the perturbing forces are acting on the satellite, making its attitude deviate from the desired one [Carrara and Kuga, 2013]. To counteract these forces, the reaction wheels will have to accelerate, and when the attitude is adjusted, the reaction wheels will stay at the reached speed. Eventually, the reaction wheel will become saturated and will not be able to reach higher speeds, and they can, therefore, no longer perform attitude manoeuvring. The reaction wheels have to unload the excess momentum and decelerate without affecting the satellite. Momentum dumping can, normally on small satellites in low Earth orbit, be done with the use of magnetorquers. This is a device consisting of a coil which, by sending current through it, produces magnetic torque when interacting with the magnetic field of the Earth. A net torque of zero can be produced by decelerating the reaction wheel and at the same time use the magnetorquer to produce a magnetic torque in the opposite direction of the torque produced with the reaction wheel [Oland and Schlanbusch, 2019]. To get a full understanding of how the reaction wheel is integrated into the attitude determination and control system an image of the Hyperion Technologies iADCS200 is included and shown in Figure 2.1.

There are several challenges involved in the design of reaction wheels for small satellites. There are limitations in volume and mass, and they must be able to operate continuously for years in space where they are subject to wide temperature variations and high radiation doses. There are two

different modes that reaction wheels are normally operated in, *current mode* (equivalently *torque mode*) and *speed mode*. In current mode, the electrical current is tracked and adjusted to achieve the desired torque. In speed mode, there is an outer control loop that eliminates the error in commanded speed by regulating the current [Carrara and Kuga, 2013].

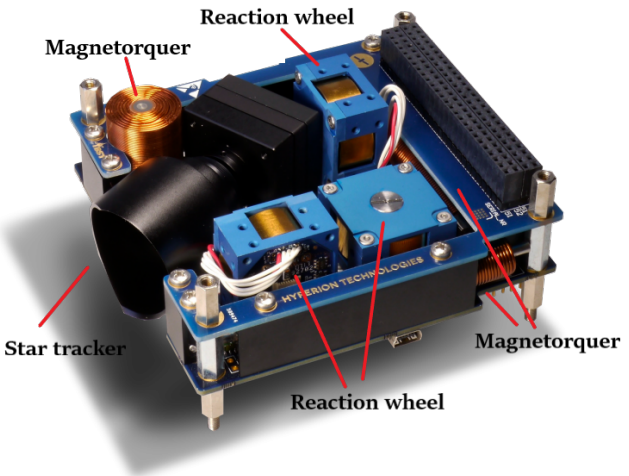

Figure 2.1: *The Hyperion Technologies iADCS200. (Image courtesy of Hyperion Technologies.)*

2.2 Brushless DC Motor

The Brushless DC motor is an electric motor. As the name suggests, brushless direct current (BLDC) motors do not have brushes, unlike the ordinary DC motors where the commutation is done mechanically with brushes. In the brushless motor, this is instead done with the use of power electronics. There are several advantages with the brushless DC motor. It has higher efficiency, reduced noise, and since you don't have brushes that gradually break, lower maintenance. Thus, it is well suited for space applications.

The electric motor consists of a rotating part, the *rotor*, and a stationary part, the *stator*. In most motors, the rotor is on the inside of the stator.

In the BLDC motor, the rotor consists of a permanent magnet with a varying amount of pole pairs. The stator consists of a varying amount of windings divided into three current paths, creating a three-phase motor. When current flows through the windings, a magnetic field will be induced. It is the interaction between this electromagnetic field and the magnetic field from the permanent magnet that is used to make the motor spin. A magnetic field with any direction and magnitude can be produced by controlling the current in the three windings. Since opposite magnet poles attract and like magnet poles repel each other the idea is to energise the phases in such a way that the permanent magnet will rotate with the electromagnetic field [Hanselman, 2006]. If the permanent magnet field is aligned with the electromagnetic field, no torque will be produced. The force produced by the interaction of the fields will then only compress the motor bearings and not cause rotation. If the stator and rotor field instead are orthogonal to each other torque will be maximised.

The stator field can be decomposed into two components, as shown in Figure 2.2. The quadrature (q) component is orthogonal to the rotor field and is the torque producing component while the direct (d) component is parallel to the rotor field and causes compression forces [John et al., 2011]. Therefore, torque will be maximised when the direct component is as small as possible. The figure also shows the basics of the electric motor construction with a permanent magnet as the rotor and windings in the stator. As mentioned before, there can be more permanent magnets and more windings in the motor, depending on the chosen design.

In the air gap between the rotor and stator, a certain magnetic flux distribution is obtained depending on the design of the motor. It depends on how the stator windings are placed, concentrated or distributed. According to Faraday's law of induction, an electromotive force (back-emf) is induced in a changing magnetic field and is equal to the negative time derivative of the magnetic flux. In an ideal motor, the back-emf shape is either perfectly trapezoidal or perfectly sinusoidal. In reality, however, these will deviate from the ideal case due to manufacturing [Hanselman, 2006].

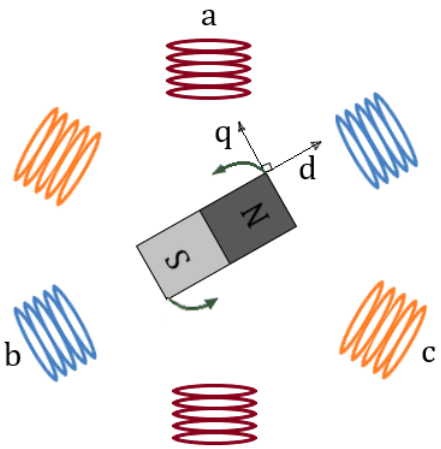

Figure 2.2: *Basic motor construction and the two stator field components.*

2.3 Reference Frames

A three-phase system is usually described by its voltage and current equations which make the analysis of such a system complex since the back-emf, induced voltages and currents change as the rotor is in relative motion. To simplify the analysis of a three-phase circuit, mathematical transformations are often used where the two most commonly used are the Clarke transformation and the Park transformation [Microsemi Corporation, 2013].

A three-phase system is described in the so-called abc-frame with 120° between the vectors, see Figure 2.3. With the Clarke transformation, these three time-domain components can be converted to two components in the orthogonal stationary, so-called $\alpha\beta$-frame. This frame is centred on the stator of the motor with the α-component aligned with the a-component of the abc-frame and the β-component orthogonal to the α-component. There are many different ways to perform this transformation where the difference is the magnitude of the two-phase quantities. There are mainly two different versions that are useful, the *power invariant* and the *amplitude invariant*

transformation. The power invariant version of the Clarke transformation can be seen in Equation 2.1. Here s denotes a general quantity which can represent a voltage, current or back-emf. The inverse of this transformation is shown in Equation 2.2.

$$\begin{cases} s_\alpha = \sqrt{\frac{3}{2}} s_a \\ s_\beta = \frac{1}{\sqrt{2}}(s_b - s_c) \end{cases} \tag{2.1}$$

$$\begin{cases} s_a = \sqrt{\frac{2}{3}} s_\alpha \\ s_b = -\frac{1}{\sqrt{6}} s_\alpha + \frac{1}{\sqrt{2}} s_\beta \\ s_c = -\frac{1}{\sqrt{6}} s_\alpha - \frac{1}{\sqrt{2}} s_\beta \end{cases} \tag{2.2}$$

The amplitude invariant version of this transform is necessary when the transform is made in analogue electronics and you want to protect the signal-to-noise ratio. In this thesis, this is the version that will be used. The amplitude invariant version of the Clarke transformation can be seen in Equation 2.3 and the inverse of it in Equation 2.4.

$$\begin{cases} s_\alpha = s_a \\ s_\beta = \frac{1}{\sqrt{3}} \cdot (s_b - s_c) \end{cases} \tag{2.3}$$

$$\begin{cases} s_a = s_\alpha \\ s_b = -\frac{1}{2} s_\alpha + \frac{\sqrt{3}}{2} s_\beta \\ s_c = -\frac{1}{2} s_\alpha - \frac{\sqrt{3}}{2} s_\beta \end{cases} \tag{2.4}$$

To transform the two time-domain components in the stationary $\alpha\beta$-frame to the rotating so-called dq-frame, the Park transformation can be used. In this frame, the d-components rotates with the electrical rotation angle θ of the motor, and the q-component is orthogonal to the d-component. The Park transformation is shown in Equation 2.5 and the inverse is shown in Equation 2.6.

$$\begin{cases} s_d = s_\alpha cos(\theta) + s_\beta sin(\theta) \\ s_q = s_\beta cos(\theta) - s_\alpha sin(\theta) \end{cases} \tag{2.5}$$

$$\begin{cases} s_\alpha = s_d cos(\theta) - s_q sin(\theta) \\ s_\beta = s_q cos(\theta) + s_d sin(\theta) \end{cases} \tag{2.6}$$

Implementing the Clarke and the Park transformation consecutively simplifies the analysis and computations of a three-phase system since the waveform of the current and voltage are converted from AC to DC signals [Alaküla et al., 2019]. Figure 2.3 shows an illustration of the three reference frames just described.

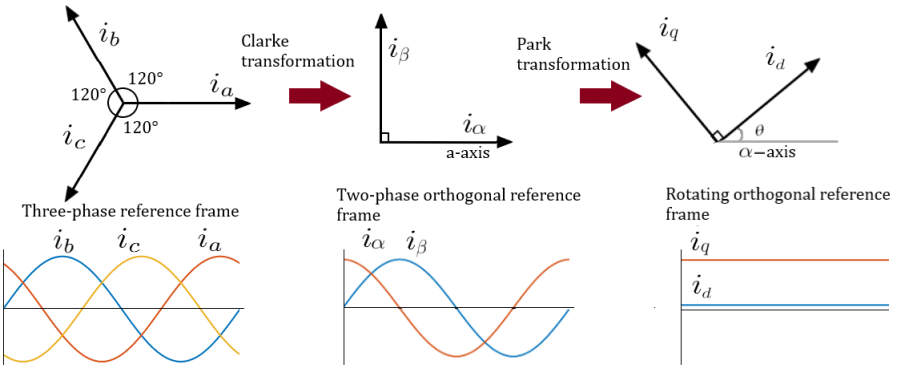

Figure 2.3: *The figure shows the three different reference frames described in this section.*

2.4 Mathematical Model

The modelling of the reaction wheel can be treated as a brushless DC motor with a high inertia mass. The BLDC motor can be described as a three-phase equivalent circuit, as shown in Figure 2.4. Each phase consists of a stator resistance R, self-inductance L and a back-emf source in series. The circuit equations for each of the windings can be expressed as shown in Equation 2.7.

$$\begin{cases} v_a = Ri_a + \frac{d}{dt}(L_{aa}i_a + L_{ba}i_b + L_{ca}i_c) + e_a \\ v_b = Ri_b + \frac{d}{dt}(L_{ab}i_a + L_{bb}i_b + L_{cb}i_c) + e_b \\ v_c = Ri_c + \frac{d}{dt}(L_{ac}i_a + L_{bc}i_b + L_{cc}i_c) + e_c \end{cases} \tag{2.7}$$

Here i_a, i_b and i_c are the currents of each phase. Assuming that the three motor phases are symmetric it follows that the three self-inductances are

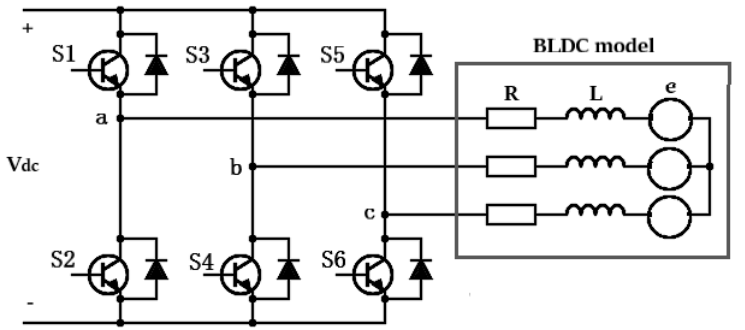

Figure 2.4: *The three-phase equivalent circuit connected to a three-phase inverter.*

equal: $L_{aa} = L_{bb} = L_{cc} = L$ and the mutual inductance too: $L_{ab} = L_{ba} = L_{ac} = L_{ca} = L_{cb} = L_{bc} = M$. Furthermore, according to Kirchoff's current law the following holds:

$$i_a + i_b + i_c = 0 \tag{2.8}$$

With these relations, the voltage equations in Equation 2.7 for the reaction wheel motor can be simplified to:

$$\begin{cases} v_a = Ri_a + (L - M)\frac{di_a}{dt} + e_a \\ v_b = Ri_b + (L - M)\frac{di_b}{dt} + e_b \\ v_c = Ri_c + (L - M)\frac{di_c}{dt} + e_c \end{cases} \tag{2.9}$$

The induced electromotive forces e_a, e_b and e_c can be described as shown in Equation 2.10. Here $f_a(\theta_e)$, $f_b(\theta_e)$ and $f_c(\theta_e)$ represents the back-emf shape of the motor as a function of the electrical angle θ_e and is limited between -1 and +1. In this thesis, the back-emf is assumed to be sinusoidal which was also confirmed through measurement. Further, K_e denotes the back-emf constant and ω_m the mechanical rotation speed of the rotor.

$$\begin{cases} e_a = f_a(\theta_e)K_e\omega_m \\ e_b = f_b(\theta_e)K_e\omega_m \\ e_c = f_c(\theta_e)K_e\omega_m \end{cases} \tag{2.10}$$

Since the phases of the motor are 120 degrees apart, f_b and f_c can be written as:

$$\begin{cases} f_b(\theta_e) = f_a(\theta_e + \frac{2\pi}{3}) \\ f_c(\theta_e) = f_a(\theta_e - \frac{2\pi}{3}) \end{cases} \tag{2.11}$$

Note that there is a difference between the electrical angular position θ_e and the mechanical angular position θ_m, which is the one that can be visualised when spinning the rotor. The relation between the two is shown in Equation 2.12 where N denotes the number of pole pairs in the rotor. This relation holds since the definition of electrical position is such that after 360 electrical degrees the rotor is back in an identical magnetic orientation. This pattern will repeat itself as many times as there are pole pairs in one mechanical revolution [Hanselman, 2006].

$$\theta_e = N\theta_m \tag{2.12}$$

Now that some of the equations for the electrical part of the reaction wheel have been defined it is possible to look at the equations for the mechanical part of the system. The equation of motion of the system will be:

$$T_e = J \cdot \frac{d}{dt}\omega_m + T_f + T_l \tag{2.13}$$

Here J is the total moment of inertia of the motor and flywheel, T_f is the friction torque and T_l is the load and disturbance torque acting on the reaction wheel. T_e represents the electromagnetic torque and is given by Equation 2.14 where K_t is the torque constant [John et al., 2011].

$$T_e = K_t(f_a(\theta_e)i_a + f_b(\theta_e)i_b + f_c(\theta_e)i_c) \tag{2.14}$$

Friction Torque

The bearing friction torque of the RW400 reaction wheel has been measured in a previous thesis project performed at Hyperion Technologies. The measurement was not performed on the same reaction wheel like the one used in this thesis, but the behaviour should be similar. This measured friction torque can be seen in Figure 2.5. It shows a clear Stribeck effect which is the behaviour that the friction torque decreases for increased velocity until

the so-called Stribeck velocity is reached. The spike that can be seen in the figure is due to this effect. A general description of the friction torque can be described as follows:

$$T_f = \begin{cases} f(v), & v \neq 0 \\ T_e, & v = 0 \wedge |T_e < T_s| \\ T_s sgn(T_e), & otherwise \end{cases} \tag{2.15}$$

Here T_e is an external torque affecting the system, which in this case is the

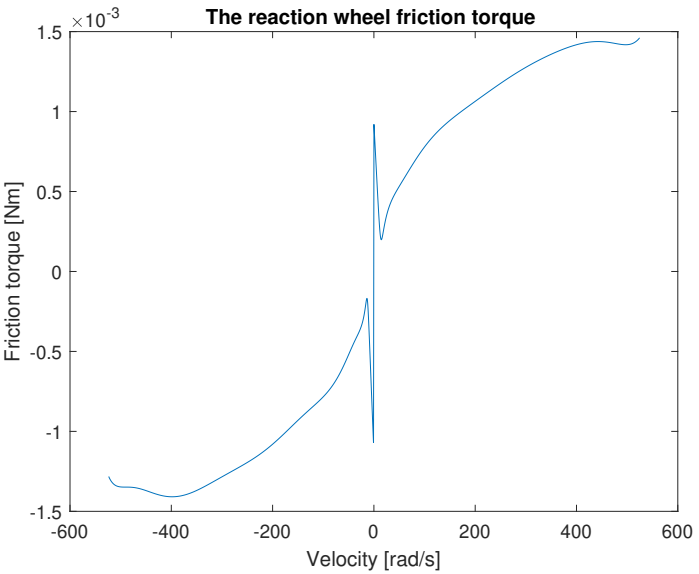

Figure 2.5: *The measured friction torque.*

electromagnetic torque, and T_s is the static friction. The reaction wheel will start rotating when the static friction is overcome. The function $f(v)$ can be described in several ways, but a common form is:

$$f(v) = T_c + T_v v + (T_s - T_c)e^{-|\frac{v}{v_s}|^2} \tag{2.16}$$

where T_c is called the Coulomb friction, T_v viscous friction and v_s the Stribeck velocity [Virgala and Kelemen, 2013]. Looking at the plot in Figure 2.5 it can, however, be seen that it has a quadratic behaviour for higher velocities so the

quadratic term, $T_x v^2$, is added to the equation. Also, a hyperbolic tangent term was added to avoid the decreasing quadratic behaviour for the higher velocities. The division by 500 was found by trial and error. Further, to get the symmetric behaviour on both half-planes, the signum function is added to the even function parts. Therefore, the equation is chosen to be:

$$f(v) = \text{sgn}(v)(T_c + T_x v^2 + (T_s - T_c)e^{-|\frac{v}{v_s}|^2}) + T_v v + T_y \tanh(\frac{v}{500}) \quad (2.17)$$

where T_x and T_y are unknown coefficients. The final step is to fit this curve to the data, and this is done with the linear least-squares method. In this way a value for T_c, T_x, T_s, T_v and T_y were found. The value for the Stribeck velocity, v_s, was found by trial and error. The result of the fitting is shown in Figure 2.6.

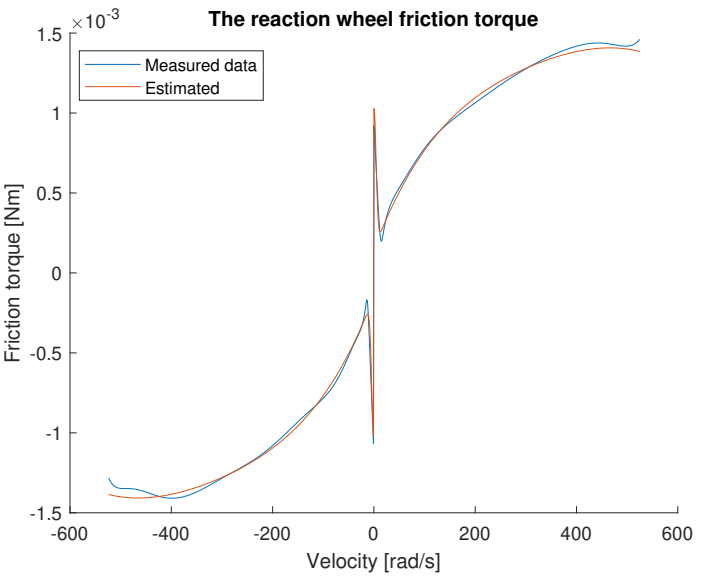

Figure 2.6: *The measured friction torque and the fitting.*

Disturbance Torque

The main source of disturbance torque is imbalance in the flywheel, which causes vibrations. The disturbance is proportional to the wheel speed squared

and can be divided into *static imbalance* and *dynamic imbalance*. These disturbances can be visualised as shown in Figure 2.7 and are a result of the production process and will differ between different reaction wheels.

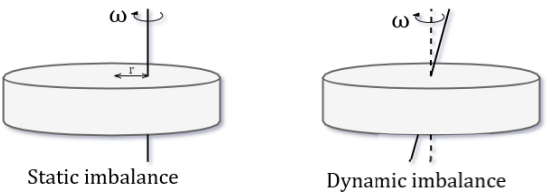

Figure 2.7: *Flywheel imbalance. Static imbalance to the left and dynamic imbalance to the right.*

The static imbalance is caused by the deviation of the centre of gravity of the flywheel from the rotation axis. The radial force caused by this imbalance is:

$$F_s = \Delta m_s R \omega^2 \tag{2.18}$$

where Δm_s is the imbalance mass that causes the disturbance and R the radius of the flywheel. If the distance from the centre of gravity is r the disturbance torque caused by the static imbalance will be:

$$T_s = \Delta m_s R r \omega^2 \tag{2.19}$$

The dynamic imbalance is caused by the misalignment between the rotation axis and the inertia direction. This disturbance torque is:

$$T_d = \Delta m_d R d \omega^2 \tag{2.20}$$

where d is the width of the flywheel and Δm_d the imbalance mass [Inamori et al., 2013]. For simplicity, the disturbance torque will not be included in the simulations for this thesis. If the wheel is well-balanced, there will not be any disturbance torque caused by imbalance. Of course, it is not possible in reality to have a perfectly balanced reaction wheel, but at least it can be assumed that the imbalance should be small.

2.5 Mathematical Model in the dq-Frame

For the analysis of the system and for the control design, it is convenient to have the electrical equations of the motor in the d/q-frame as well. Using the Clarke transformation and the Park transformation, the voltages in the d/q-frame can be obtained and will be as shown in Equation 2.21.

$$\begin{aligned} v_d &= Ri_d + L_d\frac{di_d}{dt} + e_d \\ v_q &= Ri_q + L_q\frac{di_q}{dt} + e_q \end{aligned} \tag{2.21}$$

This looks just like the equations in the abc-frame, shown in Equation 2.9. The back-emf is, however, different in the d/q-frame. The back-emf can be described as shown in Equation 2.22.

$$\begin{aligned} e_d &= -\omega_E L_q i_q \\ e_q &= \omega_E(K_e + L_d i_d) \end{aligned} \tag{2.22}$$

The inductance in the d-axis and q-axis is the same in symmetric motors, also called *non-salient* motors, which is the case in this thesis. Finally, the electromagnetic torque can be expressed as:

$$T_e = \frac{3}{2}N(\lambda i_q + (L_d - L_q)i_d i_q) \tag{2.23}$$

where λ is the magnetic flux linkage of the permanent magnet. Since it is assumed that L_d and L_q are the same, the equation of the electromagnetic torque can be simplified. Further, the torque constant K_t is defined as $N\lambda$ so Equation 2.23 can be written as:

$$T_e = \frac{3}{2}K_t i_q \tag{2.24}$$

2.6 State Estimation

To control the reaction wheel properly, the position and the speed of the rotor have to be known. This can be done either sensorless or with sensors. Sensorless control is convenient since you avoid extra hardware on the system. The accuracy, however, is not as good as with sensors. One common sensor for motor control is Hall effect sensors. The motors in the reaction

wheels at Hyperion Technologies make use of these sensors, placed 120 degrees apart from each other on the stator.

When an electric current in a conductor is placed in a magnetic field, a voltage difference called the *Hall voltage* can be measured perpendicular to the current. This is what is known as the *Hall effect*, and it is this effect that Hall sensors are based upon [Pepka, 2007]. The Hall effect sensor consists of a thin rectangular piece of a p-type semiconductor material, DC amplifiers, voltage regulators and logic switching circuits. The semiconductor can detect a magnetic field through the movement of the charge carriers in the material, creating a voltage difference. The Hall voltage is directly proportional to the strength of the magnetic field in which the semiconductor passes. [Electronics Tutorials, 2018]

The Hall effect sensor can be either linear (analogue) or digital. For linear Hall sensors, the output is obtained directly from the Hall voltage. Therefore, a continuous signal is given. The Hall sensors used in the motors at Hyperion Technologies are, however, of digital type. These kinds of Hall sensors have a Schmitt-trigger that provides hysteresis connected to the operational amplifier. With a pre-set value the output of the Hall sensor switches between its ”off” state to its ”on” state when the magnetic flux through the sensor exceeds this value. The benefit of this is that oscillation of the output signal is eliminated. The electrical position of the rotor is obtained by combining the binary signals from the three Hall sensors on the motor. The resolution of the position will be 60° [Electronics Tutorials, 2018].

2.7 Three-Phase Inverter

Since the BLDC motor is a three-phase system, a three-phase inverter is required to produce the three-phase AC voltages from a DC voltage. This is part of the hardware on the reaction wheel electronic control unit. The left part of Figure 2.4 shows the typical schematics of a three-phase inverter and how it is connected to the motor. It consists of six MOSFETs, denoted by S1

- S6, with two on each leg. The three-phase inverter is, however, not included in the simulation but just mentioned here to give a full understanding of the system. Getting an accurate simulation model is not the main focus of this thesis so to simplify the simulations, the three-phase inverter is excluded.

The output of the control algorithm driving the motor is a reference for the three-phase voltages. To generate these reference voltages through the inverter, the transistors have to know when to be ”on” and when to be ”off”. This is done through modulation of the voltage references, which is then translated to transistor signals. There are different modulation methods, but a common one used with field-oriented control is *space vector pulse width modulation* (SVPWM) which will be explained in the next chapter.

On each leg, either the top transistor is closed and the bottom transistor open or the other way around. They should never be both open or both closed since that would result in a short circuit situation. This means that there are eight different output states, also called space vectors. These can be plotted in a hexagonal star diagram, as shown in Figure 2.8. The subscript of each vector V denotes which transistor on each leg that is open. Space vector V_{100} means that the upper transistor on the first leg is open and on the other two they are closed and so on. The vectors V_{111} and V_{000} are called the zero state vectors since they don't supply any voltage. The phase voltages for different switching states can be seen in Table 2.1 [Iqbal et al., 2006].

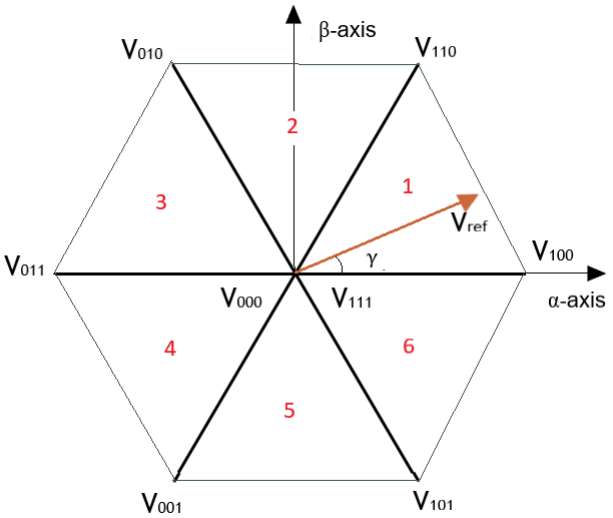

Figure 2.8: *The eight space vectors in the complex plane and the voltage reference vector* V_{ref}.

Table 2.1: *Phase voltages for different switching states.*

Switching state	**Line to neutral voltage**		
	$\mathbf{v}_a$	$\mathbf{v}_b$	$\mathbf{v}_c$
000	0	0	0
100	$(2/3)V_{dc}$	$(-1/3)V_{dc}$	$(-1/3)V_{dc}$
110	$(1/3)V_{dc}$	$(1/3)V_{dc}$	$(-2/3)V_{dc}$
010	$(-1/3)V_{dc}$	$(2/3)V_{dc}$	$(-1/3)V_{dc}$
011	$(-2/3)V_{dc}$	$(1/3)V_{dc}$	$(1/3)V_{dc}$
001	$(-1/3)V_{dc}$	$(-1/3)V_{dc}$	$(2/3)V_{dc}$
101	$(1/3)V_{dc}$	$(-2/3)V_{dc}$	$(1/3)V_{dc}$
111	0	0	0

2.8 Commutation

Commutation is the process of switching which motor phases are energised in order to generate a rotating motion of the rotor. There are different commutation methods for control of electric motors. In brushed motors, the commutation is done with brushes. In brushless motors, this is instead

done with electronics. Common electronic commutation methods are *six-step commutation*, *sinusoidal commutation* and *field-oriented control*.

Six-step commutation, also known as block commutation or trapezoidal commutation, is the simplest of the mentioned methods. This is the method that is currently used in the reaction wheels at Hyperion Technologies. The drawback of this method is that it generates torque ripple because of its nonlinear commutation scheme where only two phases are activated at each time instant. This results in a staircase looking current waveform. Sinusoidal commutation attempts to solve this by providing each of the phases with sinusoidal currents shifted 120 degrees apart. Sinusoidal commutation is, however, inefficient at high speeds since the controller has to track higher frequency sinusoidal signals. Consequently, less torque will be produced by a given amount of current [Copley Controls, n.d.]

The weakness with sinusoidal commutation is that it attempts to control the currents in a time-varying three-phase reference frame. Field-oriented control solves this by controlling the currents in the d/q-frame, where the current space vector is static, instead. Field-oriented control is therefore not limited by high frequencies since the controller is isolated from the time-varying phase currents and voltages [Copley Controls, n.d.] Six-step commutation will be briefly explained here, and field-oriented control will be explained more thoroughly in the next chapter.

Six-step commutation

In this method, two phases at a time are energised while the third one is electrically disconnected. This is done in a predetermined six-step sequence, as stated in Table 2.2. As the motor turns, information about the rotor angle is used to know when the switching between the phases should be done. The two phases that are energised are equal in magnitude, while the third one is zero. This results in six different possible directions of the current space vector. Therefore, the current waveform will be of a staircase type [Copley Controls, n.d.] These non-linearities in the commutation scheme results in a significant amount of torque ripple. This, in turn, generates noise and vibra-

tions. Further, the performance is limited from the fact that the controller has to be slow enough to not react to transients in the commutation from one phase to another [Lee and Lemley, 2009]. How the commutation pattern is related to the back-emf and rotor angle can be seen in Figure 2.9.

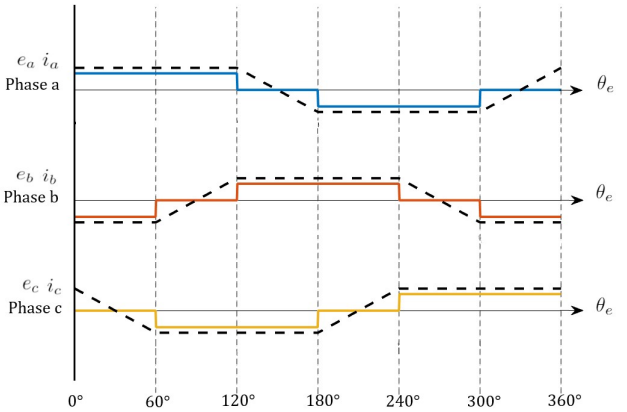

Figure 2.9: *The back-emf (here trapezoidal) and the current for the three phases depending on the rotor position.*

In summary, the commutation pattern will be as shown in Table 2.2. Both clockwise and counter-clockwise rotation of the reaction wheel is presented. In the interval 0 to 60°, phase a and b will be active while phase c will be disconnected and so on.

Table 2.2: *The commutation scheme for clockwise and counter-clockwise rotation depending on the rotor angle. a, b and c denotes the three phases.*

Rotor angle	**Clockwise rotation**			**Counter-clockwise rotation**		
	a	**b**	**c**	**a**	**b**	**c**
0° - 60°	+	-	off	-	+	off
60° - 120°	+	off	-	-	off	+
120° - 180°	off	+	-	off	-	+
180° - 240°	-	+	off	+	-	off
240° - 300°	-	off	+	+	off	-
300° - 360°	off	-	+	off	+	-

2.9 Torque Ripple

One problem with the BLDC motor is the undesired torque ripple that creates noise and mechanical vibrations which, in turn, affects the smooth performance. This is especially a problem in space applications where high accuracy is needed. Therefore, it is crucial to reduce torque ripple to improve the performance. Torque ripple is defined as periodic variations in the torque and is often presented as a percentage of the torque variations compared to the average value:

$$T_{ripple} = \frac{T_{max} - T_{min}}{T_{avg}} \cdot 100 \tag{2.25}$$

Torque ripple is caused by many different factors in the motor construction and the control strategy. Reducing torque ripple is a popular topic, and many studies have been performed focusing on this problem. One way to reduce the torque ripple is to optimise the motor structure. This would, however, increase the complexity of the design and be more expensive. The other way to reduce the torque ripple is to use more advanced motor control methods [Yuan et al., 2012], which is what this thesis is about.

Cogging torque is one cause for torque ripple. It is due to the interaction between the stator slots and the magnetic field of the permanent magnet of the rotor. This causes variations in the reluctance when the rotor changes position. This can be felt when spinning the motor by hand without any current flowing through it. Cogging torque can be avoided by using an ironless stator in the motor. Then there will be no magnetic interaction with the rotor until the controller purposely energises the windings. This kind of motor is what is used in the RW400 reaction wheel.

Another source for torque ripple is the mismatch between the waveform of back-emf and phase currents. The waveform of the phase currents is, as mentioned previously, determined by the commutation method. It can be concluded from Equation 2.14 that a bad interaction of back-emf and phase currents will result in ripples in the torque. For example, using FOC, where the currents are sinusoidal, on a motor with trapezoidal back-emf would lead

to torque ripple. Components of higher harmonics in the back-emf also result in torque ripple. Further, the theory behind six-step commutation assumes that the currents switch immediately, which in reality isn't the case. The current in the active phase will decay, and the current in the coming active phase will increase. This results in deformation in the current waveform, which consequently leads to torque ripple [Sumega et al., 2019].

3

Field-Oriented Control

With the technological improvements of semiconductors, new electronic microprocessors and digital signal processors with increased computational speed have been made possible. This has, in turn, enabled the development of effective vector control of electrical drives. Vector control is a high-performance control method that takes advantage of that the three-phase currents of the stator can be transformed into two orthogonal components visualised as a vector. Field-oriented control (FOC) is one of the best vector control methods and will be explained further in this chapter [John et al., 2011].

3.1 Fundamentals of FOC

Field-oriented control is a powerful control strategy that operates smoothly over the full speed range with less torque ripple compared to other methods. The idea behind field-oriented control is to manipulate the motor currents and voltages in the dq rotor reference frame. Consequently, the measured phase currents must be mathematically transformed to this rotating frame from the three-phase stationary reference frame. This is done with the Clarke and Park transformations that were explained in Section 2.3. The use of these transformations generally requires fast computational power. The current in the d (direct) axis is said to be the magnetic flux producing component and the current in the q (quadrature) axis the torque producing component. This means that the control of torque and flux are decoupled and can be done separately. This is usually done with PI controllers. Controlling the

current space vector in the dq frame avoids the problem with sinusoidal commutation where the current space vector is controlled in a time-variant reference frame causing limitations in the control [John et al., 2011] [Texas Instruments, 1998].

After the two currents have been processed by the controllers, a reference for the voltage has been obtained. This then has to be transformed to the three-phase reference frame with the use of the inverse Clarke and Park transform. This results in three-phase voltage signals that can be used for the pulse width modulation (PWM). A common modulation technique used with FOC is space vector pulse width modulation (SVPWM) which will be explained more in detail in Section 3.5 [John et al., 2011].

To control the speed of the motor, an outer control loop has to be implemented. This control loop provides the reference for the quadrature current, in other words, the torque reference. In summary, there is an inner loop with two current controllers and an outer loop with a speed controller. This means that the control structure is cascaded. The scheme for field-oriented control can be seen in Figure 3.1. Since SVPWM use the voltage reference in the α/β-frame the inverse Clarke transform is not really needed before the modulation and it is, therefore, not included in the figure.

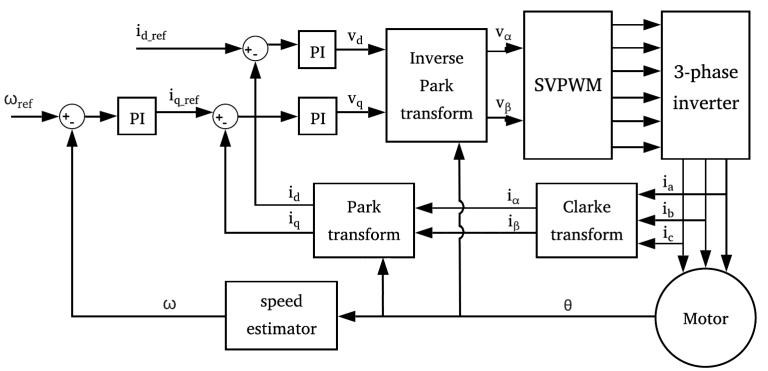

Figure 3.1: *Field-oriented control scheme.*

3.2 PI Controller

In this thesis, both the speed controller and the current controllers will use a PI controller. The PI controller is a common controller used in industry and is an acronym for Proportional and Integral. It can be described by Equation 3.1 where e is the difference between the reference signal and the process output. K_p is the proportional gain and K_i the integral gain. The first term of the equation is therefore referred to as the P-part while the second term is referred to as the I-part [Åström and Wittenmark, 2011].

$$u(t) = K_p e(t) + K_i \int^t e(s)ds \tag{3.1}$$

In the Laplace domain, the PI controller can be described as in Equation 3.2 where $U(s)$ and $E(s)$ denotes the Laplace transforms of u and e. The transfer function for the PI controller is shown in Equation 3.3.

$$U(s) = K_p E(s) + \frac{K_i}{s} E(s) \tag{3.2}$$

$$G_{PI}(s) = \frac{K_p s + K_i}{s} \tag{3.3}$$

To implement a digital controller this equation has to be discretised. There are different discretisation methods, but the forward difference is most commonly used for approximating the I-part. The P-part is purely static and thus does not require an approximation. The discretised P-part and I-part are shown in Equation 3.4 where h denotes the sampling interval and kh the sampling instance.

$$\begin{cases} P(kh) = K_p e(kh) \\ I(kh+h) = I(kh) + K_i h e(kh) \end{cases} \tag{3.4}$$

In physical systems, actuators can be saturated, meaning that they have reached the limit of their performance. When using integral action in the controller, the undesirable effect integrator windup will happen when the actuator saturates. When the control error is so large that the integrator causes the actuator to saturate, the integral part may accumulate to large

values. When the error is finally reduced, the integral part may be so large that it takes time for the integrator to reach a normal value again. This will give a poor response of the system.

There are different ways to avoid integrator windup. In this thesis, the method called *back-calculation* will be used as the anti-windup method. In this method, an extra feedback path is introduced with an output from an actuator model. The difference between the output from the actuator model and the controller output forms an error signal e_s. This is then fed back to the integrator through a gain K_b. When the actuator is not in the saturated region, the error signal will be zero and when the actuator is saturated, this error signal will be used to reset the integrator. With this anti-windup method, the I-part will then be as shown in Equation 3.5 [Åström and Wittenmark, 2011].

$$I(kh + h) = I(kh) + K_i he(kh) + K_b he_s(kh) \tag{3.5}$$

3.3 Current Controllers

The controller for the quadrature current needs a torque reference, and the controller for the direct current needs a flux reference. To maximise the produced torque, the direct current reference is set to zero since it is only the quadrature current that produces useful torque. Setting the direct current reference to zero will drive the current space vector to be solely in the quadrature direction [John et al., 2011]. Sometimes the direct current reference is set different from zero in a process called *field weakening*. This is necessary when the motor is intended to operate at speeds higher than the nominal speed. Since the induced voltage is dependent on rotation speed, it might exceed the maximum allowed output voltage when the speed gets high, and that would affect the performance. Field weakening will prevent this from happening [Alaküla et al., 2019]. This will not be necessary for this thesis since the back-emf will not be a limiting factor in the reaction wheel.

Using the equations for the motor model in the dq-frame described in Section 2.5, a simplified transfer function of the plant from voltage to current

can be derived. This transfer function is shown in Equation 3.6. Here it is assumed that the back-emf is constant. This is a reasonable assumption since it usually changes very slowly with respect to the current as it is dependent on the speed of the motor. A simplified version of the inner control loop can be seen in Figure 3.2. It is also important to note that the inner control loop is much faster than the outer control loop, since it handles the electrical part of the motor, and can therefore be tuned first.

$$G_i(s) = \frac{1}{L_{q/d}s + R} \tag{3.6}$$

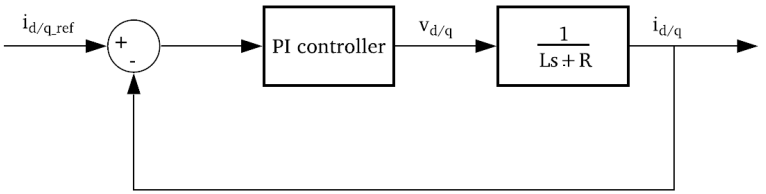

Figure 3.2: *Block diagram of the inner control loop.*

Using the transfer function of the PI controller presented in Equation 3.3 the closed-loop system will be:

$$G_{cl}(s) = \frac{K_P s + K_I}{Ls^2 + (R + K_P)s + K_I} \tag{3.7}$$

One way to tune the controller is described by Wilson (2015). Here the poles are chosen to be real and the zero introduced by the PI controller cancelled. This is also the method that is used for the automatic tuning in the VESC-Tool, that will be used for the evaluation of FOC on the real reaction wheel. The VESC and the VESC-Tool will be introduced in Chapter 4. The resulting gains for the PI-controller are:

$$\begin{aligned} K_P &= L \cdot \text{bandwidth} \\ K_I &= R \cdot \text{bandwidth} \end{aligned} \tag{3.8}$$

To compensate for the back-emf induced in the motor, a feedforward path can be introduced to the controller to improve the performance. This is done in the dq-frame. Therefore, the back-emf presented in Equation 2.22 is used for the compensation.

3.4 Speed Controller

The speed controller needs a speed reference as an input. A simplified version of the outer control loop can be seen in Figure 3.3.

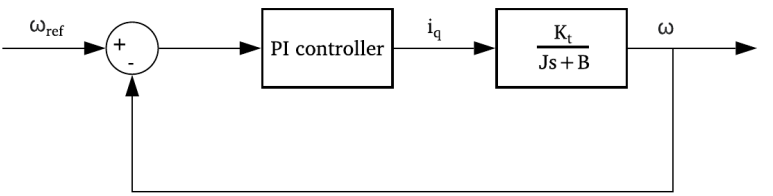

Figure 3.3: *Block diagram of the outer control loop.*

A simplified transfer function of the motor dynamics can be obtained by assuming that the friction only consists of a viscous term and that there is no imbalance in the reaction wheel. Using Equation 2.13 and Equation 2.24 the transfer function will be as in Equation 3.9.

$$G_m(s) = \frac{K_t}{J_{tot}s + B} \tag{3.9}$$

With the PI controller presented in equation 3.3 the closed loop system will be as seen in Equation 3.10.

$$G_{cl}(s) = \frac{K_p K_t s + K_I K_t}{J_{tot}s^2 + (B + K_P K_t)s + K_I K_t} \tag{3.10}$$

3.5 Space Vector Pulse Width Modulation

Space Vector Pulse Width Modulation (SVPWM) is a modulation technique used for control of the voltage source inverter to generate the desired voltages

to the three phases of the motor. This is the final step in the field-oriented control scheme. SVPWM provides a lower harmonic distortion and more efficient use of the supply voltage compared to other common modulation methods [John et al., 2011]. This will not be included in the simulation but it is, however, used in the VESC firmware and will therefore be explained here.

The idea is to use the eight space vectors explained in Section 2.7 to rebuild the reference voltage vector, here denoted by V_{ref}. The reference voltage vector is constructed from the voltage references in the α/β-frame, obtained from the two current controllers. Depending on the location of V_{ref} in the star diagram, the desired voltage is constructed from the two adjacent space vectors and one zero vector. The length of one space vector is dependent on time. Therefore, V_{ref} is constructed by letting one active vector remain for some time, T_1, followed by the next active vector during the time, T_2. The time that remains, T_0, of one switching period, T_s, is used for the zero vectors, half of the time for V_0 and half of the time for V_7 [John et al., 2011]. These time durations can be calculated using Equation 3.11 where γ is the angle of the voltage reference vector and n the value of the sector that V_{ref} is currently in [Djup and Allar, 2015], see Figure 2.8.

$$\begin{aligned} T_1 &= \frac{\sqrt{3}T_s|V_{ref}|}{V_{dc}} sin(\frac{\pi}{3}n - \gamma) \\ T_2 &= \frac{\sqrt{3}T_s|V_{ref}|}{V_{dc}} sin(\gamma - \frac{\pi}{3}(n-1)) \\ T_0 &= T_s - T_1 - T_2 \end{aligned} \tag{3.11}$$

The recreated version of the voltage vector can then be expressed as in Equation 3.12. Here V_x is one of the 6 active space vectors and V_{x+60° the adjacent space vector.

$$V_{ref,recreated} \approx \frac{T_1}{T_s}V_x + \frac{T_2}{T_s}V_{x+60^\circ} + \frac{T_0}{T_s}(V_0 \text{ or } V_7) \tag{3.12}$$

The conventional SVPWM method requires large computational power due to all the complex calculations. A simplified version of the SVPWM is proposed by Srikanth and Dutt (2012). Their method avoids all the complex

trigonometric calculations and instead consists of logical variables and operations, making it suitable for digital implementation. Their method will now be presented.

The first step is to convert the reference voltages v_a, v_b, v_c to the amplitude invariant α/β-frame, using the inverse Clarke transformation presented in equation 2.3, in order to identify in which sector the reference vector lies. The following algorithm can be used to determine the sector where v_{ref1}, v_{ref2}, v_{ref3} are intermediate variables. A, B, C are logical variables which are either 0 or 1 depending on the condition stated in Equation 3.14. With these logical variables, the variable N can be determined, which is used to map to the sector P.

$$\begin{cases} v_{ref1} = v_\beta \\ v_{ref2} = \frac{\sqrt{3}}{2} v_\alpha - \frac{1}{2} v_\beta \\ v_{ref3} = -\frac{\sqrt{3}}{2} v_\alpha - \frac{1}{2} v_\beta \end{cases} \tag{3.13}$$

$$\begin{aligned} &\text{If} \quad v_{ref1} > 0 \quad A = 1 \quad \text{else} \quad A = 0 \\ &\text{If} \quad v_{ref2} > 0 \quad B = 1 \quad \text{else} \quad B = 0 \\ &\text{If} \quad v_{ref3} > 0 \quad C = 1 \quad \text{else} \quad C = 0 \end{aligned} \tag{3.14}$$

$$N = A + 2B + 4C \tag{3.15}$$

The variable N can be mapped into the sector P where the reference vector lies using Table 3.1. However, note that in the further calculations, the variable N will be used and not P.

Table 3.1: *The mapping of variable N to sector P.*

P	1	2	3	4	5	6
N	3	1	5	4	6	2

The next step is to calculate the action times, T_1 and T_2, of the two basic vectors in the sector. Instead of using space angles and trigonometry to calculate these values as presented in Equation 3.11, they are calculated using v_α and v_β. First, the intermediate variables X, Y and Z, as defined in Equation 3.16, are calculated. These can then be mapped to the action times, T_1 and

T_2, using Table 3.2.

$$\begin{cases} X = \sqrt{3}v_\beta T_s / V_{dc} \\ Y = T_s(3v_\alpha + \sqrt{3}v_\beta)/(2V_{dc}) \\ Z = T_s(-3v_\alpha + \sqrt{3}v_\beta)/(2V_{dc}) \end{cases} \tag{3.16}$$

Table 3.2: *The mapping of X, Y, Z to action times* T_1 *and* T_2.

N	3	1	5	4	6	2
T_1	-Z	Z	X	-X	-Y	Y
T_2	X	Y	-Y	Z	-Z	-X

If $T_1 + T_2$ is bigger than the time of one switching period, T_s, the action times are adjusted according to Equation 3.17.

$$\begin{aligned} T_1 &= T_1 T_s/(T_1 + T_2) \\ T_2 &= T_2 T_s/(T_1 + T_2) \end{aligned} \tag{3.17}$$

With the action times known it is now time to determine T_a, T_b and T_c which corresponds to the time comparison values of each phase. First the intermediate variables T_{aon}, T_{bon} and T_{con} are calculated according to Equation 3.18. These values can then be mapped to T_a, T_b and T_c with Table 3.3.

$$\begin{cases} T_{aon} = \frac{(T_s - T_1 - T_2)}{4} \\ T_{bon} = T_{aon} + \frac{T_1}{2} \\ T_{con} = T_{bon} + \frac{T_2}{2} \end{cases} \tag{3.18}$$

Table 3.3: *The mapping of* T_{aon}, T_{bon} *and* T_{con} *to* T_a, T_b *and* T_c.

N	3	1	5	4	6	2
T_a	T_{aon}	T_{bon}	T_{con}	T_{con}	T_{bon}	T_{aon}
T_b	T_{bon}	T_{aon}	T_{aon}	T_{bon}	T_{con}	T_{con}
T_c	T_{con}	T_{con}	T_{bon}	T_{aon}	T_{aon}	T_{bon}

The final step is to generate the PWM signals. This is done by comparing T_a, T_b and T_c with an isosceles triangle carrier wave with magnitude $T_s/2$ and period $2T_s$. A typical view of how these signals look can be seen in Figure 3.4. If T_a is bigger than the carrier wave the upper transistor gate denoted S1 in Figure 2.4 will be activated, and if T_a is smaller than the carrier wave the lower transistor (S2) on that phase leg will be activated. In the same way, T_b and T_c are compared to the carrier wave and the corresponding transistor signals are then obtained.

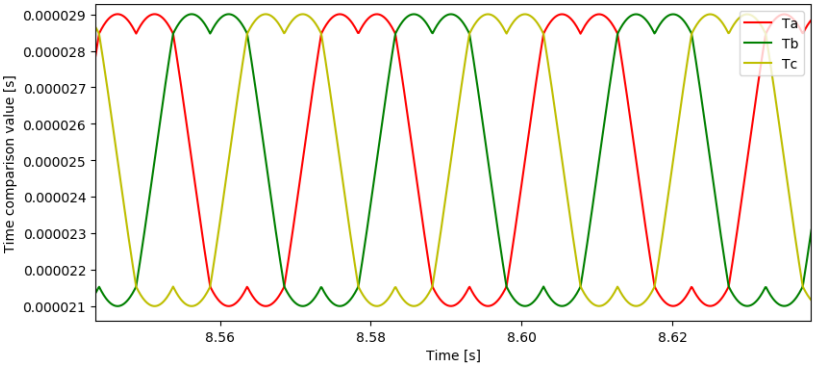

Figure 3.4: *Space vector modulated waveforms.*

4

Implementation

To evaluate the performance of the reaction wheel driven by FOC this has to be implemented on the real system. To save time, an already made electronic speed controller (ESC) with FOC was used. The ESC used was the so-called VESC which will be explained in this chapter together with the procedure to get a working reaction wheel driven with this ESC.

4.1 Introduction to VESC

Vedder's electronic speed controller (VESC) is an open-source motor controller introduced by the Swedish engineer Benjamin Vedder. It was originally developed for handmade electric skateboards but has been used in other projects as well. Both the hardware and the firmware are open-source, which makes it easy to modify as desired by the user. The VESC supports both field-oriented control and six-step commutation [Vedder, 2016].

The VESC is easy to use as there is a powerful GUI, called the VESC-Tool, where the settings can easily be modified, and the firmware can be updated. Also, the current, speed and position can be tracked with real-time graphs in the GUI. With a USB cable, the VESC can be connected to the computer, and the VESC-Tool can be used to set up the motor controller. There are tests in the VESC-Tool that can be used to find the motor settings. Figure 4.1 shows the initial page of the VESC-Tool [Vedder, 2020].

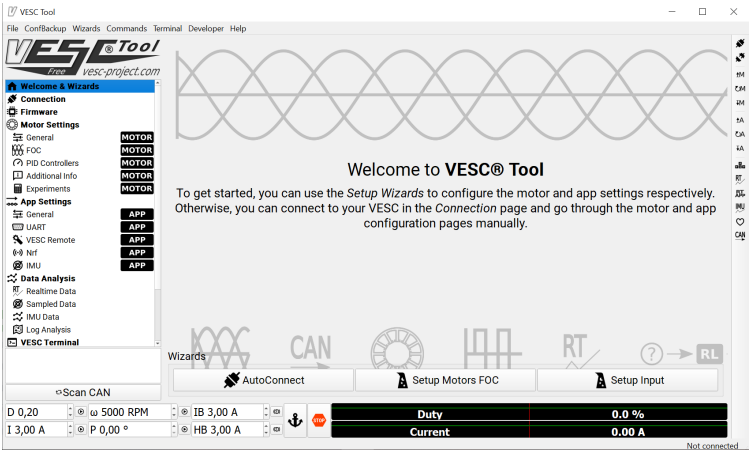

Figure 4.1: *Start page of the VESC Tool.*

The VESC used in this thesis is the Flipsky mini FSESC4.20. This hardware, together with any other VESC, is as mentioned intended for electric skateboards that usually use a lot more current than a small satellite reaction wheel. To get an accurate measurement of the currents, the shunt resistors, that are a part of the current sensing, were changed from 1mΩ to 10mΩ. The front and back of the ESC can be seen in Figure 4.2.

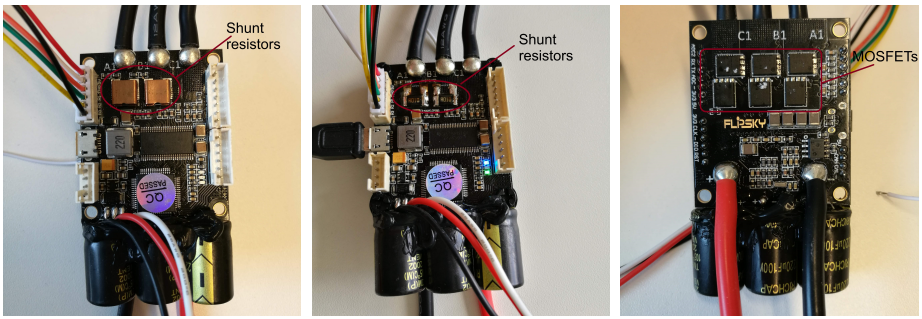

(a) *The front of the VESC with shunt resistors of 1mΩ.*

(b) *The front of the VESC with shunt resistors of 10 mΩ*

(c) *The back of the VESC with the six MOSFETs.*

Figure 4.2: *The VESC used in this thesis.*

4.2 Running the Reaction Wheel with VESC

To run everything the VESC is connected to a power supply, and the reaction wheel is connected to the VESC. Further, the VESC is connected to the laptop with a USB cable. Figure 4.3 and Figure 4.4 show the setup with the VESC, reaction wheel, power supply and laptop. The VESC needs at least 8V to operate, however, the reaction wheel should not have more voltage than 7V. This is solved by altering the maximum duty cycle in the VESC-Tool. The power supply was set to 10V, and the maximum duty cycle set to 70%. In this way, the reaction wheel voltage will be limited to 7V.

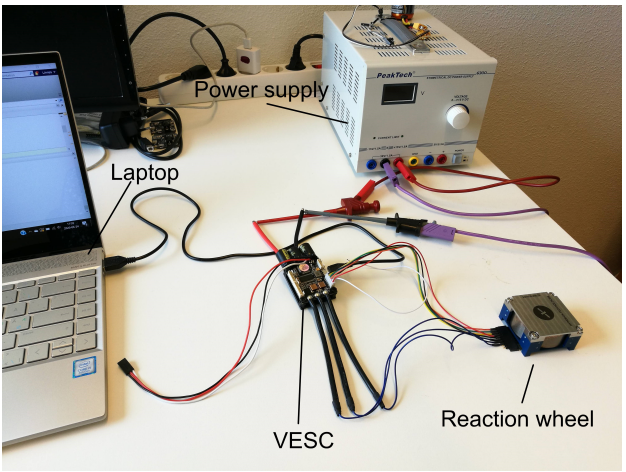

Figure 4.3: *The setup showing the laptop, VESC, reaction wheel and power supply.*

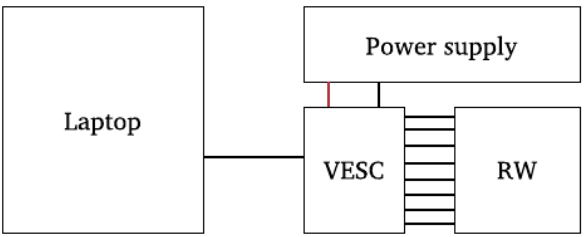

Figure 4.4: *A diagram of the setup.*

4.3 Hall Sensor Table

For the controller to know the speed of the motor and the position of the rotor, the placement of the Hall sensors has to be known. The settings for this can be altered in the FOC tab in the VESC-Tool. Here the electrical rotation speed, given in rotations per minute (rpm), for when the controller should switch to sensorless mode instead of using hall sensors for state estimation can also be set. This value is set to be above the operating speed since the Hall sensors should be used in the full speed range in this case.

The Hall table can be determined automatically using the VESC-Tool. The result is shown in Table 4.1. The values correspond to the rotor angle but with one revolution being 200° instead of 360°.

Table 4.1: *The Hall table used in the VESC.*

Hall entry	**Hall table**
1	133
2	67
3	100
4	200
5	167
6	33

4.4 Current Controller Tuning

The next step was to tune the controllers. For the current controllers, the VESC-Tool tunes them automatically with the known motor resistance and inductance. This is done as explained in Section 3.3. With the bandwidth set to 1000 Hz, the PI gains resulted in a very noisy behaviour in the reaction wheel. Changing the bandwidth to 100 Hz gave a better result, however, the current tracking was not as fast. Therefore, the PI gains were tweaked and the final values chosen were:

$$K_p = 0.01$$

$$K_i = 500$$

4.5 Alterations in the Firmware

Before proceeding with proper tuning of the speed controller, the anti-windup method in the VESC firmware was changed. The original method only consisted of a truncation of the I-term between -1 and 1, which did not give a satisfactorily result. The speed step response gave a typical integral windup overshoot with this method as can be seen in Figure 4.5. Therefore, it was altered to the method back-calculation explained in Section 3.2.

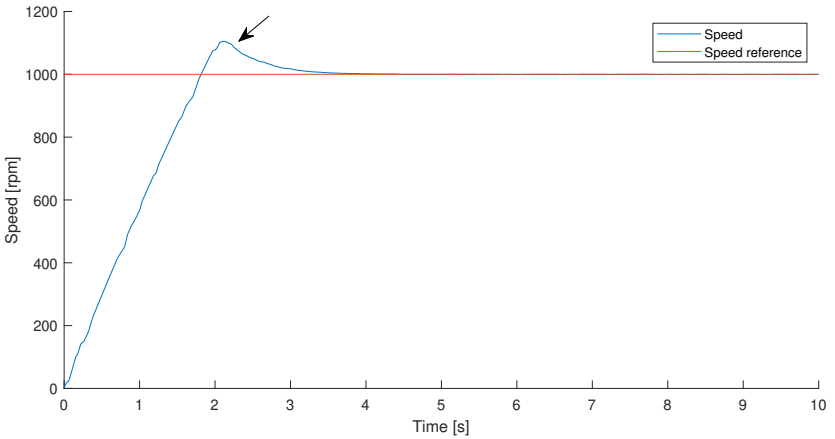

Figure 4.5: *Integral windup in the speed step response.*

Further, the gains in the speed controller in the firmware were divided by 20. This was removed as it didn't really have any purpose here.

4.6 Speed Controller Tuning

Lastly, the speed controller had to be tuned. To find a good starting point for the tuning, the *Ziegler-Nichols tuning rule* was used. The Ziegler-Nichols tuning rule consists of setting the integral gain to zero and then change the proportional gain until the system starts to oscillate with stable and consistent oscillations. The gain where this happens is called the ultimate gain and higher gains than the ultimate gain will give diverging oscillations.

The ultimate gain K_u and the oscillation period T_u are used to determine the PI gains. The rules for the gains are presented in Equation 4.1 [Hägglund, 2000].

$$\begin{aligned} K_p &= \frac{K_u}{2.2} \\ K_i &= \frac{1.2K_p}{T_u} \end{aligned} \tag{4.1}$$

With this method, the ultimate gain became $K_u = 0.004395$ and the oscillation period approximately $T_u = 0.398$. A plot of this is shown in Figure 4.6. Through the tuning rules in Equation 4.1, the PI gains area $K_p = 0.002$ and $K_i = 0.00602$.

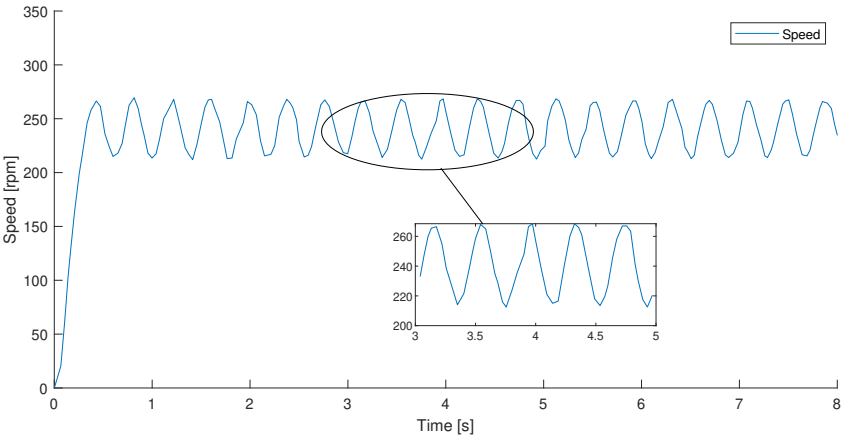

Figure 4.6: *Plot showing the consistent oscillations.*

This gave more overshoot in the step response than what was desired, as shown in Figure 4.7, so the gains were tweaked to get a satisfactory response. The final values used were $K_p = 0.0013$ and $K_i = 0.00113$, and the back-calculation coefficient was set to 10. These gains did, however, only give the desired response when using a step size of 1000 rpm. For higher steps, there was still some overshoot. Therefore, gain scheduling is necessary to get a consistent response in the full speed range. Not much time was spent on this, so the quick solution to this was to tweak the integral gain for different steps

by trial-and-error. This was then fitted to a quadratic function using the fitting tool in Matlab and then implemented on the VESC.

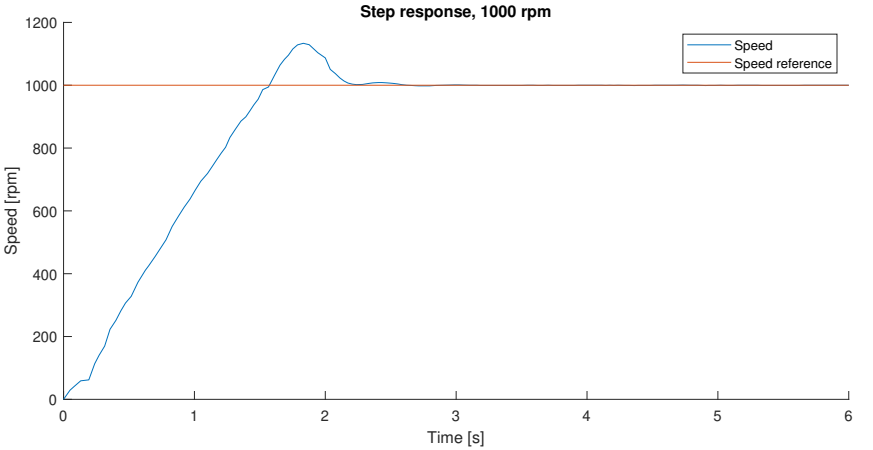

Figure 4.7: *Step response using the PI gains obtained through the Ziegler-Nichols tuning rule.*

5

Experiments and Results

In this chapter, the results from the simulations and the implementation on the reaction wheel will be presented. Results both from using six-step commutation and from using field-oriented control will be shown. In the first section, the results from the Python simulations are presented and in the second section, the results from the hardware implementation are presented in terms of step responses. In the final section, the results from the micro-vibration measurements are presented.

5.1 Results from the Python Simulation

To evaluate the performance of the two control methods, a few step responses were performed. These step responses were chosen to be 1000 rpm, 3000 rpm and 5000 rpm. Since the satellite weighs more than the reaction wheel itself, the reaction wheel will have to spin much faster than the speed needed for the satellite to adjust its attitude. In the extreme case, the reaction wheel would have to go from a low to a high speed and therefore the step of 5000 rpm is one of the chosen step sizes, where 5000 rpm is considered high for this reaction wheel. The other two step responses were chosen to be able to compare the performance for a few different speeds.

Field-Oriented Control

The step response for a step of 1000 rpm, 3000 rpm and 5000 rpm together with the corresponding net torque are presented in Figure 5.1, Figure 5.2 and Figure 5.3 respectively. The step response plot is shown to the left, and the

torque is shown to the right. When speaking of rpm, it will be the mechanical rpm that is being referred to and not the electrical rpm.

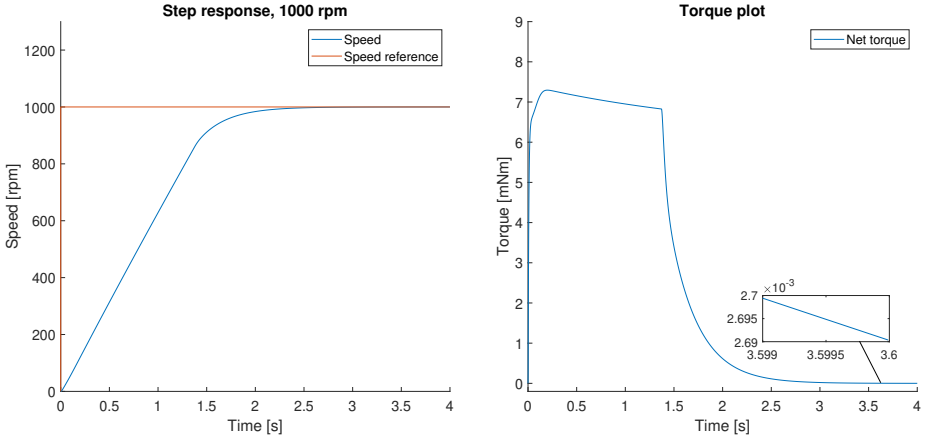

Figure 5.1: *The plot to the left shows the step response with a step size of 1000 mechanical rpm, and the plot to the right shows the torque and a magnified view of it when using field-oriented control.*

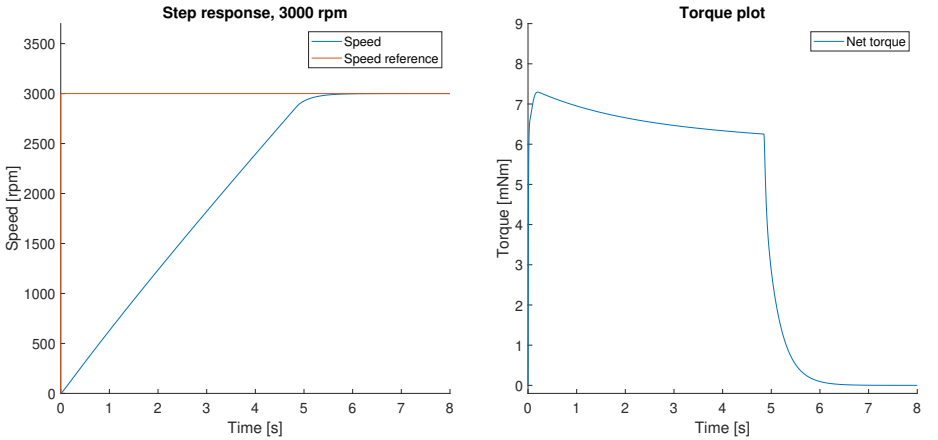

Figure 5.2: *The plot to the left shows the step response with a step size of 3000 mechanical rpm, and the plot to the right shows the torque when using field-oriented control.*

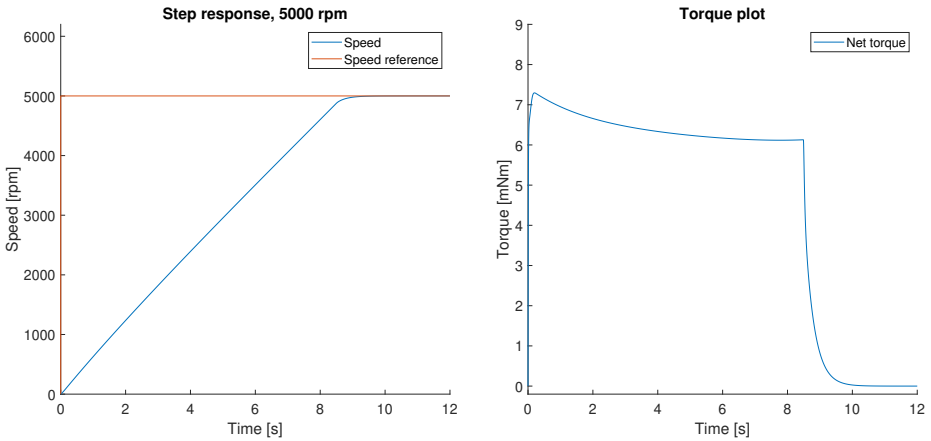

Figure 5.3: *The plot to the left shows the step response with a step size of 5000 mechanical rpm, and the plot to the right shows the torque when using field-oriented control.*

The time it takes for the response to rise from 10% to 90% of the steady-state value (rise time), the time it takes for the error to fall within 2% of the final value (settling time) and the percentage of overshoot for the three step responses is presented in Table 5.1. The torque ripple is also presented here and is obtained through Equation 2.25. The maximum current in the three cases was 0.99A.

Table 5.1: *Step response characteristics and the torque ripple when using field-oriented control.*

	1000 rpm	**3000 rpm**	**5000 rpm**
Rise time [s]	1.30	4.07	7.02
Settling time [s]	1.94	5.06	8.55
Overshoot [%]	0	0	0
Torque ripple [%]	0	0	0

To evaluate the performance of the inner control loop, a plot of the direct current and the quadrature current is shown in Figure 5.4. In this case, the speed step is set to 3000 rpm. The upper plot shows the direct current control and the lower plot shows the quadrature current control.

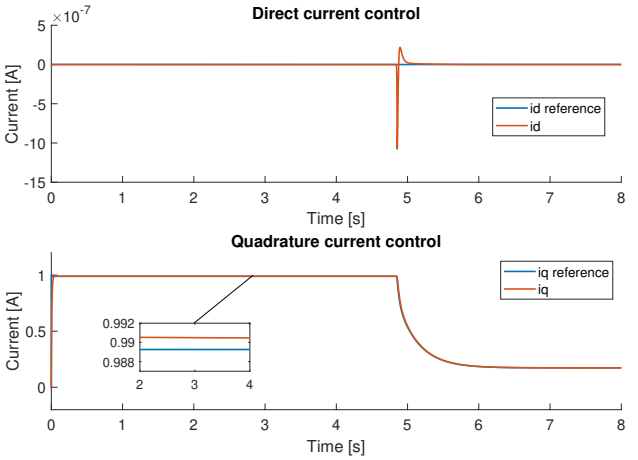

Figure 5.4: *The response of the current controllers in the field-oriented control scheme. The plot on the top shows the direct current control and the plot on the bottom shows the quadrature current control.*

Six-step commutation

Simulations were also performed using six-step commutation. The step response for a step of 1000 rpm, 3000 rpm and 5000 rpm together with the corresponding torque are presented in Figure 5.5, Figure 5.6 and Figure 5.7 respectively.

As with FOC, the step response characteristics are calculated. The rise time, the settling time and the percentage of overshoot for the three step responses are presented in Table 5.2. The torque ripple is also presented here. The maximum current in the three cases was approximately 1.16A.

Table 5.2: *Step response characteristics and the torque ripple when using six-step commutation.*

	1000 rpm	**3000 rpm**	**5000 rpm**
Rise time [s]	1.16	3.99	8.60
Settling time [s]	1.93	6.74	11.33
Overshoot [%]	0	0	0
Torque ripple [%]	8.04	47.58	52.65

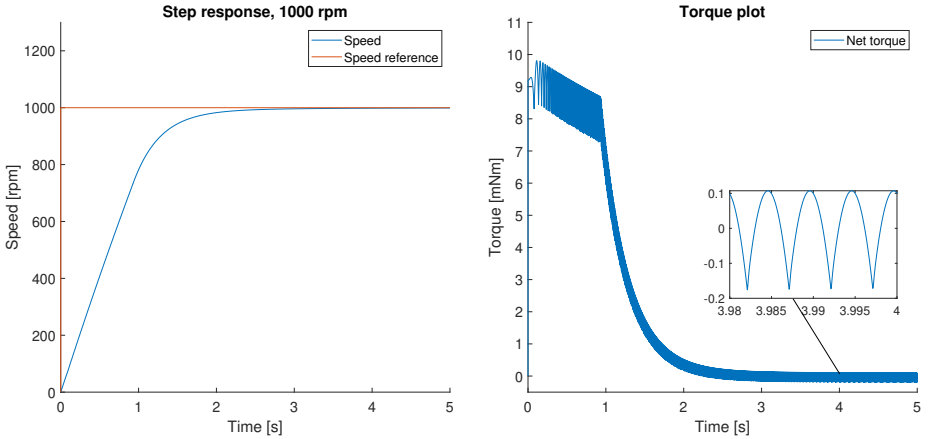

Figure 5.5: *The plot to the left shows the step response with a step size of 1000 mechanical rpm, and the plot to the right shows the torque and a magnified view of it when using six-step commutation. Here the torque ripple is visible and has approximately the frequency 200Hz.*

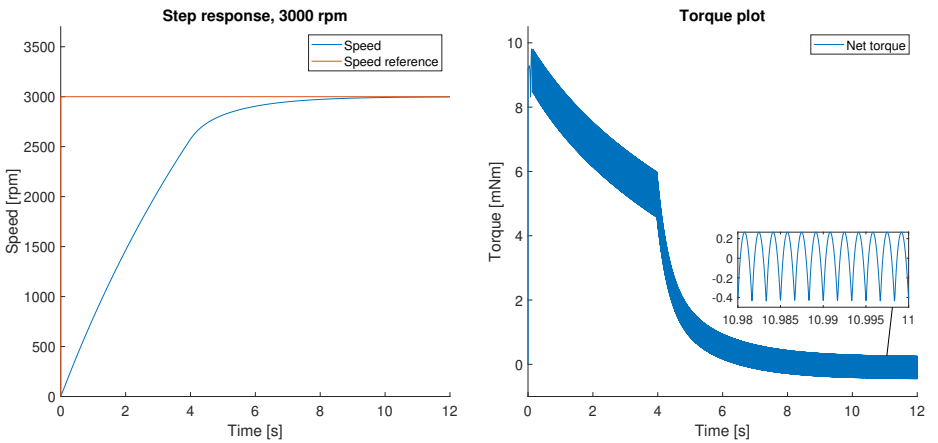

Figure 5.6: *The plot to the left shows the step response with a step size of 3000 mechanical rpm, and the plot to the right shows the torque and a magnified view of it when using six-step commutation. Here the torque ripple is visible and has approximately the frequency 600Hz.*

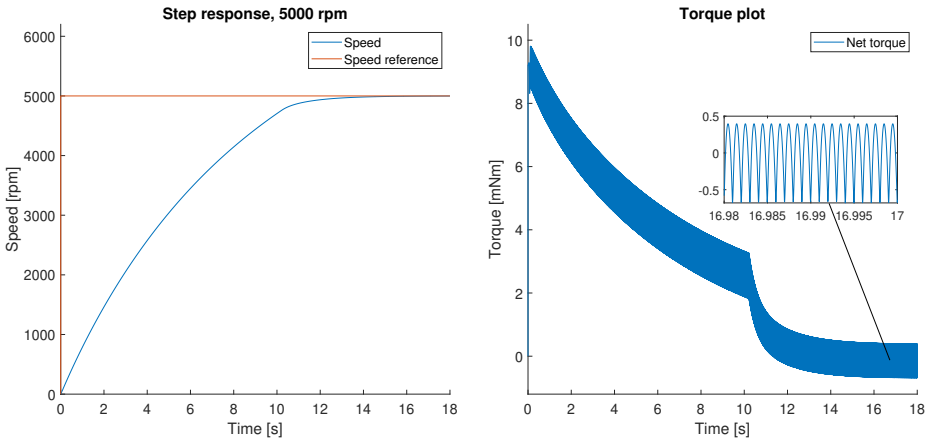

Figure 5.7: *The plot to the left shows the step response with a step size of 5000 mechanical rpm, and the plot to the right shows the torque and a magnified view of it when using six-step commutation. Here the torque ripple is visible and has approximately the frequency 1000Hz.*

5.2 Results from the Hardware Implementation

In this section, the results from the real reaction wheel are presented. The experiments were performed with the current reaction wheel controller at Hyperion Technologies, henceforth referred to as the HT controller, and using the VESC implementation. The step responses that were performed in the simulations were also performed here.

Another thing that was evaluated was the performance of the reaction wheel when crossing zero rpm. Reaction wheels tend to have a poor performance when passing through zero speed. This can be explained by the static friction that has to be overcome before the motor starts spinning. During large slew manoeuvres of the satellite, zero-crossings are important [Magner, 2018]. Therefore, this is an interesting region to look into. The step response sequence that was chosen was to set the speed reference from 0 rpm to 3000 rpm and then to -3000 rpm and finally back to 0 rpm.

VESC with Field-Oriented Control

The step response of a step of 1000 rpm, 3000 rpm and 5000 rpm together with the corresponding control signal are presented in Figure 5.8, Figure 5.9 and Figure 5.10 respectively.

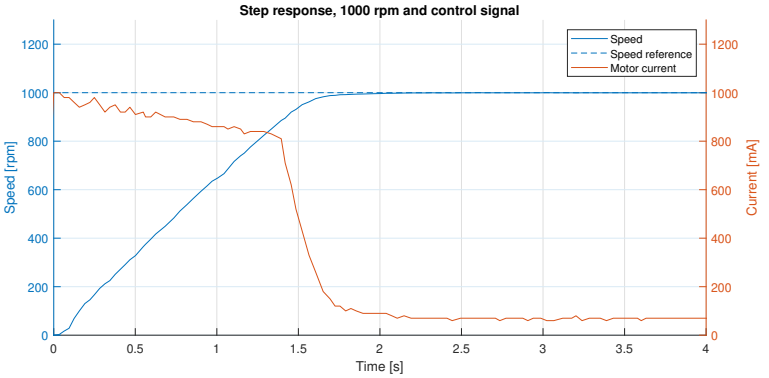

Figure 5.8: *The step response with a step size of 1000 mechanical rpm and the corresponding control signal when using the VESC with field-oriented control.*

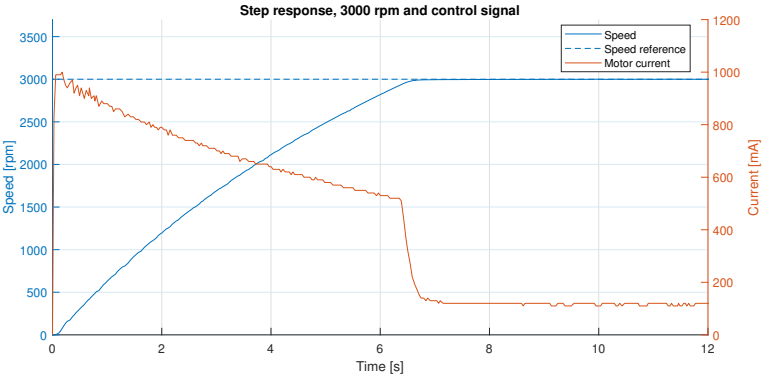

Figure 5.9: *The step response with a step size of 3000 mechanical rpm and the corresponding control signal when using the VESC with field-oriented control.*

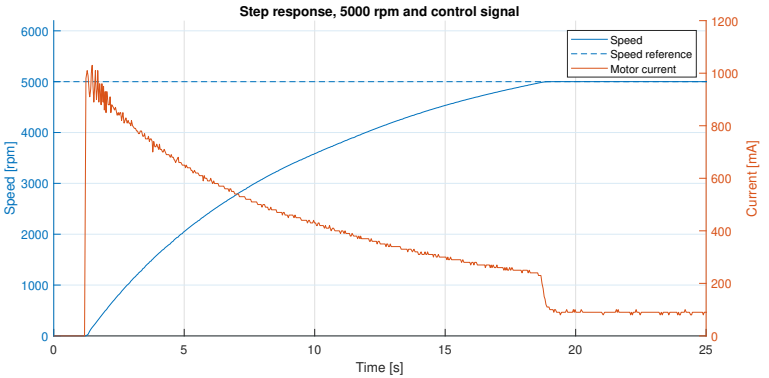

Figure 5.10: *The step response with a step size of 5000 mechanical rpm and the corresponding control signal when using the VESC with field-oriented control.*

The rise time, settling time and percentage of overshoot for the three different step responses are presented in Table 5.3.

Table 5.3: *The step response characteristics when using the VESC with field-oriented control.*

	1000 rpm	**3000 rpm**	**5000 rpm**
Rise time [s]	1.27	5.11	12.79
Settling time [s]	1.6	6.28	16.66
Overshoot [%]	0.05	0.017	0.03

Lastly, a step response sequence was performed where a zero-crossing was included. The speed reference went from 0 rpm to 3000 rpm to -3000 rpm and finally back to 0 rpm. The response, together with the corresponding control signal, is shown in Figure 5.11.

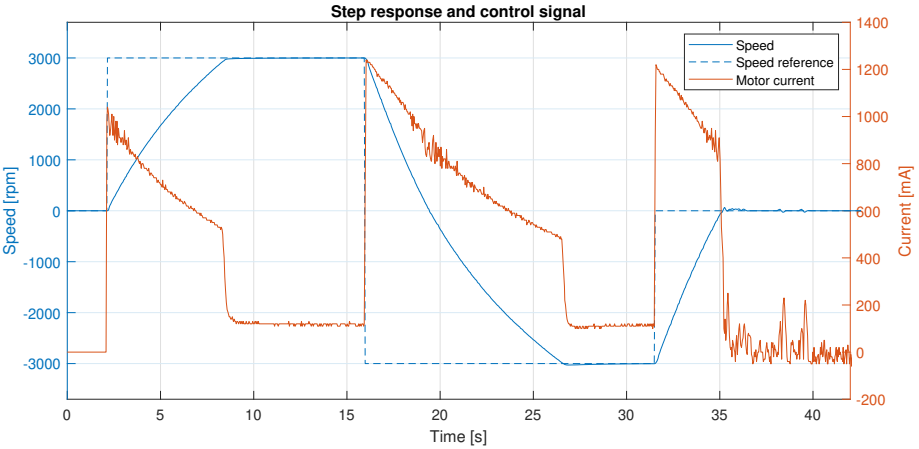

Figure 5.11: *Step response sequence with zero speed crossing and the corresponding control signal when using the VESC with field-oriented control.*

The HT Controller with Six-Step Commutation

The step response of a step of 1000 rpm, 3000 rpm and 5000 rpm together with the corresponding control signals are presented in Figure 5.12, Figure 5.13 and Figure 5.14 respectively.

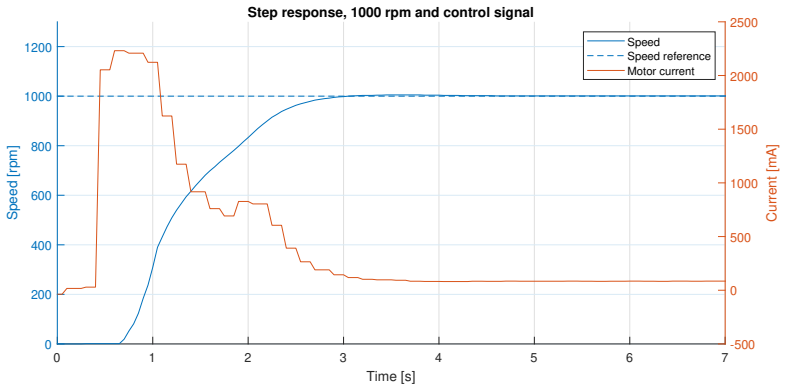

Figure 5.12: *The step response with a step size of 1000 mechanical rpm and the corresponding control signal when using the Hyperion Technologies controller with six-step commutation.*

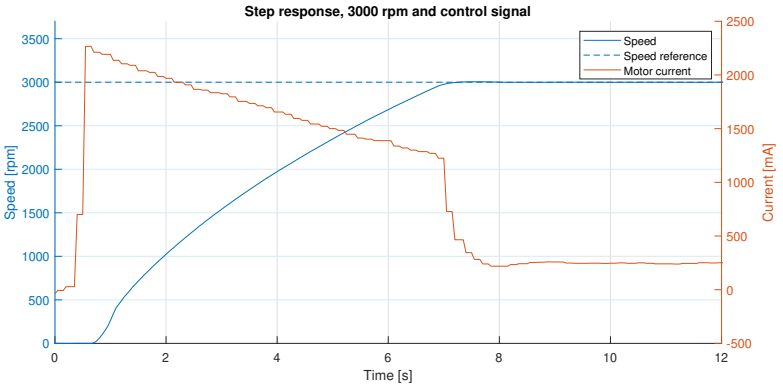

Figure 5.13: *The step response with a step size of 3000 mechanical rpm and the corresponding control signal when using the Hyperion Technologies controller with six-step commutation.*

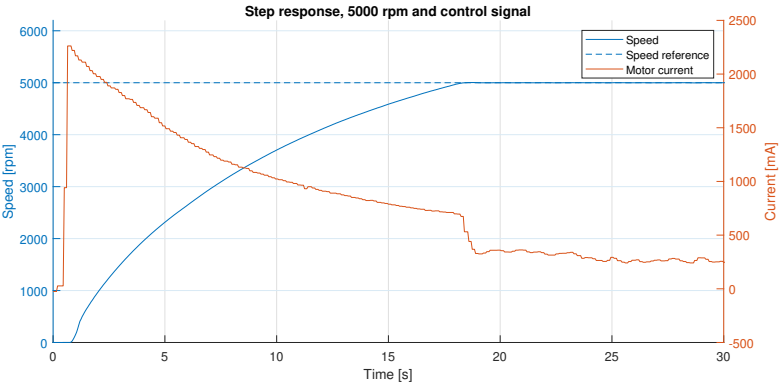

Figure 5.14: *The step response with a step size of 5000 mechanical rpm and the corresponding control signal when using the Hyperion Technologies controller with six-step commutation.*

The rise time, settling time and percentage of overshoot for the three different step responses are presented in Table 5.4.

Table 5.4: *The step response characteristics when using the Hyperion Technologies controller with six-step commutation.*

	1000 rpm	**3000 rpm**	**5000 rpm**
Rise time [s]	1.38	5.02	13.11
Settling time [s]	2.66	6.84	17.42
Overshoot [%]	0.5	0.17	0.08

The same step response sequence that was performed with VESC was performed with the HT controller. The result is shown in Figure 5.15.

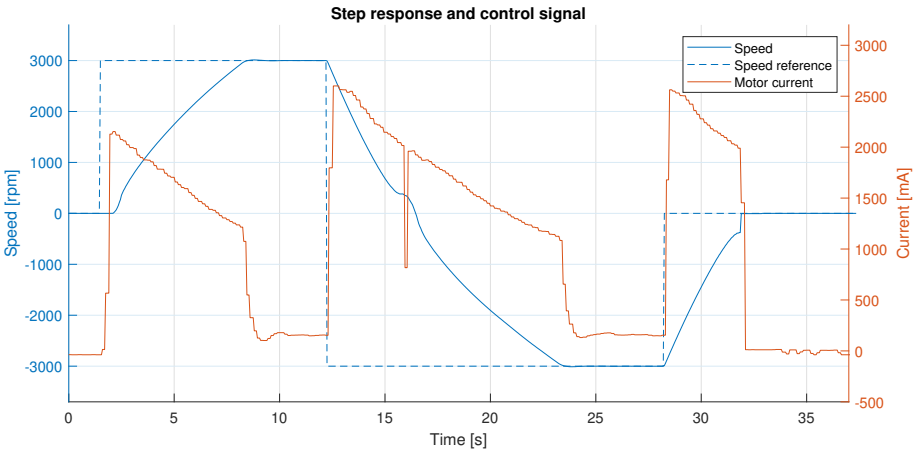

Figure 5.15: *Step response sequence with zero speed crossing and the corresponding control signal when using the Hyperion Technologies controller with six-step commutation.*

5.3 Vibration Testing

The final experiment performed was a vibration test. This was done using a Kistler multi-component dynamometer type 9129AA where both forces and torques can be measured in all three axes. The reaction wheel was mounted on the dynamometer, as shown in Figure 5.16. The data was sampled at 700 Hz. Before running the reaction wheel, a background measurement was performed with the reaction wheel mounted on the dynamometer and one

without the reaction wheel on the plate. Some of the resonance modes in the vibration tests will come from the surroundings and not from the reaction wheel itself. Therefore, to distinguish these modes, the background measurement is needed.

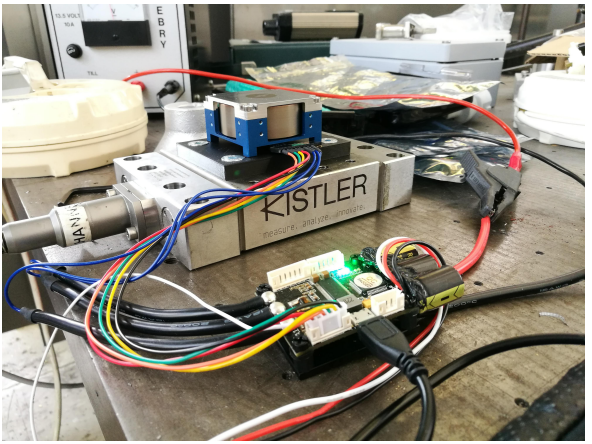

Figure 5.16: *The reaction wheel mounted on the Kistler dynamometer and connected to the VESC.*

Initially, the idea was to generate so-called waterfall plots to visualise the vibrations by accelerating the reaction wheel to full speed but to do this a higher sampling frequency is required, which was not possible with the available acquisition system. Data was instead being recorded for about 4 minutes at a few different rpm levels. This was done with the VESC controller and the HT controller. The data was then used to generate power spectral density (psd) plots to visualise the difference between the two controllers.

The result when spinning the reaction wheel at a few constant rpm levels can be seen in Figure 5.17. The plots show the moment in the z-axis since this is where the motor commutation torque ripple will be visible. From the plots, it can observed that the background measurement is quite large, making it difficult to distinguish the background data from the reaction wheel data. One problem with the setup of the Kistler table is that it is in a workshop where heavy machines are operating and interfering with the

vibrations of the reaction wheel. Ideally, you would want a vibration free surrounding.

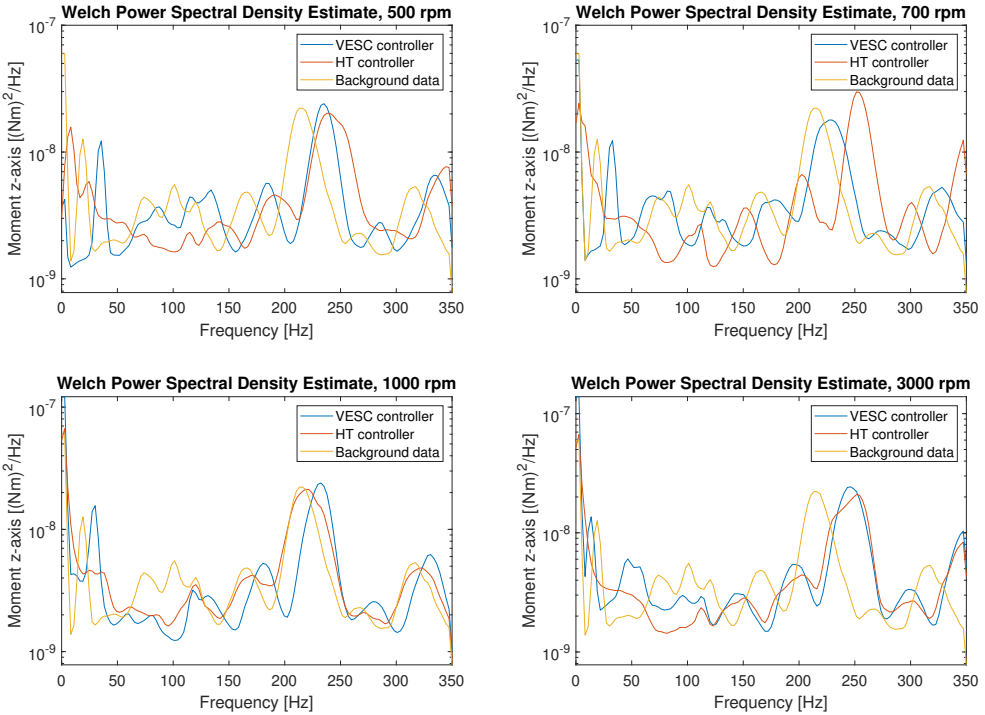

Figure 5.17: *Power Spectral Density plots from running the reaction wheel at 500, 700, 1000 and 3000 mechanical rpm. The blue plot corresponds to using the VESC controller, the red plot corresponds to the current Hyperion Technologies controller and the yellow plot is the background data.*

A background measurement was also performed later in the evening when people had gone home so that fewer machines would be operating at the time of the measurement. A measurement with the reaction wheel spinning on the Kistler plate was also performed to see if it would be possible to distinguish this new background data from the reaction wheel data. A plot of the results

from the evening measurement can be seen in Figure 5.18. The plot shows the previous background measurement, the new background measurement and the result when the reaction wheel was spinning at 1000 rpm.

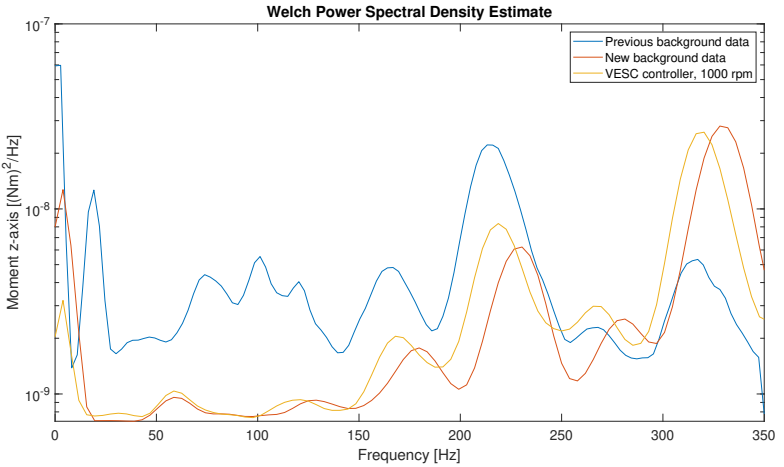

Figure 5.18: *Comparison of background data performed at two different times during the day. The blue plot is the background data seen in Figure 5.17, the red plot is the new background data and the yellow plot is the reaction wheel data at 1000 rpm. The new background data i smaller at low frequencies, however, the reaction wheel data can still not be distinguished from the background.*

6

Discussion

This chapter begins with a discussion of the results presented in the previous chapter. First, a discussion of the performance of the two different controllers will be presented, followed by a discussion of the vibrations. Finally, the chapter ends with some suggestions for future work.

6.1 Controller Performance

Starting with the Python simulations, it can be observed from Table 5.1 and Table 5.2 as well as in the step response plots in Figure 5.1- Figure 5.7 that the performance of the two controllers is quite similar for low speed but differ more for higher speeds. The step response is slightly faster with FOC. Further, it can be seen in Figure 5.4 that the current controllers perform well. The quadrature current follows the reference nicely with only a very small offset. The same applies to the direct current. The spike that occurs after almost 5 seconds is because of the sudden change in the quadrature current, but it is still very close to zero when compared to the quadrature current. This behaviour can also be observed in the results from the real reaction wheel. The reason that this is happening is that the control signal from the speed control is saturated at first, and when the control error is getting smaller the control signal will leave the saturated region. This results in this abrupt change in quadrature current and is also the reason why the speed control has a sudden change in behaviour as in Figure 5.7 at around 11s. Another thing to note is that the controller with six-step commutation uses more current than the controller with FOC. Since current and torque are

proportional, this also leads to six-step commutation producing more torque.

When comparing the results from the real reaction wheel presented in Table 5.3 and Table 5.4 it can be observed that the controller with FOC is slightly faster than the controller with six-step commutation. Also, the overshoot is slightly lower with the VESC controller, but this is probably more due to the implementation of the speed control and not the commutation method itself. Looking at the plots presented in Figures 5.8, 5.9, 5.10, 5.12, 5.13 and 5.14 one can observe the difference in the control signal. First of all, it can be observed that FOC needs much less current to have similar and even better performance than six-step commutation. Secondly, it is clear here that FOC has a much smoother performance at lower speeds. The control signal with the Hyperion Technologies controller at a step of 1000 rpm is much more uneven compared to the same case but with the VESC. This also leads to the speed looking rough at the step of 1000 rpm with the HT controller. At higher speeds, this is not the case. This agrees well with theory which says that six-step commutation is deficient at low speeds while FOC performs well in the full speed range. The main reason that FOC has a more efficient use of current, faster step response and smoother behaviour in the full speed range is that FOC can produce any voltage input vector. This means that the maximum torque can always be produced theoretically. Six-step commutation, on the other hand, can only produce six different voltage input vectors, meaning that torque is only maximised six times per electrical revolution. Therefore, the current is not used as efficiently as with FOC, and this could also be the reason that the uneven behaviour at the step response of 1000 rpm can be seen. This is also the reason why more torque ripple is produced with six-step commutation, as can be seen in the results from the simulation. The uneven behaviour at a step of 1000 rpm with the HT controller could also be explained by some filtering issue in their implementation.

It's also interesting to look at the performance when crossing zero rpm. Looking at Figure 5.11 and Figure 5.15, it is clear that the controller with FOC is much smoother when going from positive to negative rpm. Looking at the corresponding control signal, it can be seen that the HT controller has

a sudden spike to negative current just before the zero speed crossing. This would explain the uneven behaviour in the step response. The reason that this current spike is happening is probably that the controller loses control when the speed estimation gets less and less accurate when approaching zero speed. It quickly catches up, however, but with the consequence that the speed response is less smooth. The small jump at about 32 seconds in Figure 5.15 could also be explained with the speed tracking not being very accurate at low speeds.

Finally, the noisy control signal with the VESC, that can be seen especially in Figure 5.3 and Figure 5.11, needs to be addressed. Close to zero speed, the control signal is very noisy. This is not the case with HT controller. This could perhaps be improved by changing the shunt resistors on the VESC. Before changing the shunt resistors in the initial stage of the implementation, the current was even noisier. Another thing that could explain this behaviour is the inaccuracy in the speed estimate at low speeds. The controller will then have trouble around zero rpm, resulting in the noisy current. Unfortunately, since the current is this noisy, it should also result in more torque ripple since these two are proportional.

6.2 Vibrations

When looking at the Python simulations and comparing the result from field-oriented control and six-step commutation, presented in Table 5.1 and Table 5.2 as well as in the plots presented in Figure 5.1 - Figure 5.3 and Figure 5.5 - Figure 5.7, it is clear that FOC results in far less torque ripple than six-step commutation. The torque ripple in the FOC case is 0% which in reality wouldn't happen. The reason that the torque is looking perfect in this case is that the back-emf in the simulation is set to be perfectly sinusoidal. When producing perfectly sinusoidal currents, there will not be any torque ripple. If the back-emf would deviate from a perfect sinusoid, there would be torque ripple, and this is the case in reality. In the case with six-step commutation, there is instead a lot of torque ripple which is a result of having staircase looking current waveforms with sinusoidal back-emf. Even

if the back-emf would be more of a trapezoidal type, there would still be torque ripple. The torque ripple due to commutation will be zero only when the back-emf and current waveforms match. Torque ripple can also be caused by the motor construction but since no imbalance or other disturbances were included in the simulations, this is not seen in the plots.

Unfortunately, the results from the simulation can not be confirmed by real measurements since the measurement setup was not ideal for micro-vibration measurements. The background noise that could be seen in Figure 5.17 could come from the ventilation system or other machines operating continuously. The problem with the measurement could also be due to some kind of internal problem in the measurement equipment. This equipment is probably meant for measurements of higher forces where the background noise is considered small relative to the measured signal. Even when performing the measurement later in the evening when fewer machines were operating, there was a problem distinguishing the reaction wheel data from the background data, as seen in Figure 5.18. It is, therefore, clear that it is difficult to get a proper measurement of the vibrations. If one were to perform the measurement properly, however, the result should be as predicted in theory with reduced torque ripple and therefore reduced micro-vibrations when using FOC. Comparing Figure 5.10 with Figure 5.14 it, however, looks like the torque ripple at low speeds in the FOC case should be greater than with six-step commutation since the current is quite noisy around zero speed. When the speed has reached its desired value, the current looks much smoother and doesn't really give any hints of high torque ripple. As already mentioned, the noisy current could be due to the speed estimation or due to a hardware problem. Either way, it's difficult to draw any conclusions of the torque ripple in the real implementation without proper measurements.

6.3 Future Work

The first thing that should be done is to measure the micro-vibrations and compare the two controllers based on that. It is unfortunate that it was not possible to perform the measurement in this thesis. Getting data on this

would be really interesting and should be the first step in continuing this work. Before doing this, though, it could be a good idea to look into why the current in the VESC is noisy at low speeds. Otherwise, this could interfere with the vibration measurements, suggesting that FOC leads to more vibrations when the noisy current isn't necessarily caused by the commutation method.

The FOC controller as it is now is far from being a finished product. The VESC is way too large to be put on a CubeSat class reaction wheel. The next step would be to investigate how to incorporate FOC on the reaction wheel. Also, the gain scheduling in the speed control needs to be given some more focus before implementing this on a real product. FOC could also advantage from a more accurate position sensor. Clearly, the Hall sensors worked well but to achieve better results at low speeds an encoder could be used. Implementing an encoder in the reaction wheel is already being worked on by another thesis student at Hyperion Technologies.

To get a better understanding of the system, the simulation could be evolved by adding the influence of the Hall sensors, the three-phase inverter and modulation as well as the imbalance of the wheel. This is not the most important thing to focus on as the simulation as it is already tells a lot about the performance of FOC, but perhaps it could be interesting for other work.

Another suggestion for future work is to implement Iterative Learning Control to reduce the torque ripple further. This is done by Jayabaskaran et al. (2013) where the torque ripple was reduced by a big amount using this method. Although FOC alone already reduces the ripples a lot, in theory, this could be a further improvement.

7

Conclusions

The aim of this thesis was to evaluate whether field-oriented control would improve the performance and reduce the vibrations of the Hyperion Technologies RW400 reaction wheel that currently uses six-step commutation. First, the two different control methods were simulated in Python. From the results of the simulations, it can be concluded that using FOC will improve the performance and result in less torque ripple, and therefore less micro-vibrations, when compared to six-step commutation.

Further, the control method was also tested on the real reaction wheel. The Hyperion Technologies reaction wheel controller was compared to the open-source VESC with FOC through step responses and vibration measurements. The results here also suggests that FOC is the better alternative as the control is faster and smoother through zero speed and since the current is used more efficiently. Since the vibration measurement was not successful, no conclusion can be made from this in the real implementation but, theoretically, there should be less torque ripple.

In summary, it can be concluded that it would be an improvement for Hyperion Technologies to implement field-oriented control in their reaction wheels. At least when it comes to the control performance and efficiency, and it will most likely also reduce the vibrations due to torque ripple. The computational power would, however, be greater and the implementation more difficult but if that is not a limitation, FOC is a great choice.

Bibliography

Alaküla, M., P. Karlsson, and H. Bängtsson (2019). *Power Electronics: Devices, Converters, Control and Applications*. Lund University.

Åström, K. J. and B. Wittenmark (2011). *Computer-Controlled Systems*. Dover Publications.

Carrara, V. and H. Kuga (2013). "Estimating friction parameters in reaction wheels for attitude control". *Mathematical Methods Applied to the Celestial Mechanics of Artificial Satellites 2013*. DOI: https://doi.org/10.1155/2013/249674.

Copley Controls (n.d.). *What is 'field oriented control' and what good is it?* URL: https://www.maccon.de/fileadmin/redaktion/downloads/Produkte/Antriebselektronik/Copley_drives/Field-Oriented-Control.pdf. (accessed: 20.06.2020).

Djup, M. and E. Allar (2015). "Sensorless control of brushless dc motor in hydraulic application". *Lund University*.

Electronics Tutorials (2018). *Hall effect sensor*. URL: https://www.electronics-tutorials.ws/electromagnetism/hall-effect.html. (accessed: 10.06.2020).

Hanselman, D. (2006). *Brushless Permanent Magnet Motor Design*. Magna Physics Publishing.

Hägglund, T. (2000). *REGLERTEKNIK AK Föreläsningar*. Institutionen för reglerteknik.

Inamori, T., J. Wang, P. Saisutjarit, and S. Nakasuka (2013). "Jitter reduction of a reaction wheel by management of angular momentum using magnetic torquers in nano- and micro-satellites". *Advances in Space Research* **52**, pp. 222–231. DOI: 10.1016/j.asr.2013.02.014.

Iqbal, A., A. Lamine, I. Ashraf, and Mohibullah (2006). "Matlab/simulink model of space vector pwm for three-phase voltage source inverter". In: pp. 1096 –1100. ISBN: 978-186135-342-9. DOI: 10.1109/UPEC.2006.367646.

Jayabaskaran, G., B. Adhavan, and V. Jagannathan (2013). "Torque ripple reduction in permanent magnet synchronous motor driven by field oriented control using iterative learning control with space vector pulse width modulation". In: *2013 International Conference on Computer Communication and Informatics*, pp. 1–6.

John, P. J., S. S. Kumar, and B. Jaya (2011). "Space vector modulation based field oriented control scheme for brushless dc motors". *2011 International Conference on Emerging Trends in Electrical and Computer Technology*, pp. 346–351. DOI: 10.1109/ICETECT.2011.5760141.

Lee, S. and T. Lemley (2009). "A comparison study of the commutation methods for the three-phase permanent magnet brushless dc motor". *Electrical Manufacturing Technical Conference 2009: Electrical Manufacturing and Coil Winding Expo*, pp. 49–55.

Lopes, R., V. Carrara, and H. Kuga (2019). "Stepwise modeling with friction/inertia effects separation and velocity control with dynamic compensation of a reaction wheel". *Computational and Applied Mathematics* **38**:20, pp. 1–11. DOI: https://doi.org/10.1007/s40314-019-0784-x.

Magner, R. D. (2018). "Extending target tracking capabilities through trajectory and momentum setpoint optimization". In:

Microsemi Corporation (2013). *Park, inverse park and clarke, inverse clarke transformations mss software implementations user guide*. URL: https://www.microsemi.com/document-portal/doc_view/132799-park-inverse-park-and-clarke-inverse-clarke-transformations-mss-software-implementation-user-guide. (accessed: 24.05.2020).

Mohamad Fakhari, M., S. Hilmi, and M. A. M. Ali (2015). "Developing a proposed satellite reaction wheel model with current mode control". *Proceeding of the 2015 International Conference on Space Science and Communication (IconSpace)*.

Oland, E. and R. Schlanbusch (2019). "Reaction wheel design for cubesats". *2009 4th International Conference on Recent Advances in Space Technologies*, pp. 778–783. DOI: 10.1109/RAST.2009.5158296.

Pepka, G. (2007). "Position and level sensing using hall-effect sensing technology". *Sensor Review* **27**, pp. 29–34. DOI: 10.1108/02602280710723442.

Srikanth, V. and A. A. Dutt (2012). "Performance analysis of a permanent magnet synchronous motor using a novel svpwm". *2012 IEEE International Conference on Power Electronics, Drives and Energy Systems (PEDES)*, pp. 1–6. DOI: 10.1109/PEDES.2012.6484445.

Sumega, M., Zoššák, P. Varecha, and P. Rafajdus (2019). "Sources of torque ripple and their influence in bldc motor drives". *Transportation Research Procedia* **40**, pp. 519–526. DOI: https://doi.org/10.1016/j.trpro.2019.07.075.

Texas Instruments (1998). *Field orientated control of 3-phase ac-motors*. URL: https://www.ti.com/lit/an/bpra073/bpra073.pdf. (accessed: 26.05.2020).

Vedder, B. (2016). *Vesc – open source esc*. URL: http://vedder.se/2015/01/vesc-open-source-esc/. (accessed: 15.08.2020).

Vedder, B. (2020). *Vesc tool*. URL: https://vesc-project.com/vesc_tool. (accessed: 15.08.2020).

Virgala, I. and M. Kelemen (2013). "Experimental friction identification of a dc motor".

Wilson, D. (2015). *Teaching your pi controller to behave part ii*. URL: https://e2e.ti.com/blogs_/b/industrial_strength/archive/2015/07/20/teaching-your-pi-controller-to-behave-part-ii. (accessed: 17.06.2020).

Yuan, Y., F. Auger, L. Loron, S. Moisy, and M. Hubert (2012). "Torque ripple reduction in permanent magnet synchronous machines using angle-based

iterative learning control". In: *IECON 2012 - 38th Annual Conference on IEEE Industrial Electronics Society*, pp. 2518–2523.

Lund University
Department of Automatic Control
Box 118
SE-221 00 Lund Sweden

Document name
MASTER'S THESIS

Date of issue
December 2020

Document Number
TFRT-6119

Author(s)
Linnéa Rosenbecker

Supervisor
Bert Monna, Hyperion Technologies, Sweden
Anders Robertsson, Dept. of Automatic Control, Lund University, Sweden
Kristian Soltesz, Dept. of Automatic Control, Lund University, Sweden (examiner)

Title and subtitle

Vibration Attenuation for Satellite Reaction Wheels through the use of Field-Oriented Control

Abstract

Complex space components are getting more important as the request for high precision space missions is increasing. The main contribution to vibrations on a satellite is the reaction wheels, the primary actuator in the attitude control of the satellite. One of the main sources of vibrations is torque ripple which is caused by various reasons, one being the control algorithm. This thesis focuses on reducing the vibrations in the reaction wheels at Hyperion Technologies by using a more complex motor control algorithm known as field-oriented control (FOC) instead of six-step commutation that is currently used. The reaction wheel driven with FOC was simulated in Python before testing the concept on the real reaction wheel. The open-source electronic speed controller VESC was used to evaluate the performance of the reaction wheel driven with FOC. The results from the simulations showed that it would be a significant improvement to use FOC, both when it comes to torque ripple and control performance. Due to some difficulties with the vibration measurement setup, the torque ripple aspect of the controller could not be confirmed in real life. It has, however, been shown that the reaction wheel would greatly advantage from using FOC instead of six-step commutation when it comes to the control performance.

Keywords

Classification system and/or index terms (if any)

Supplementary bibliographical information

ISSN and key title
0280-5316

ISBN

Language
English

Number of pages
1-72

Recipient's notes

Security classification

http://www.control.lth.se/publications/